Rotation Equivariant Mamba for Vision Tasks

Zhongchen Zhao, Qi Xie, Keyu Huang, Lei Zhang, Deyu Meng, and Zongben Xu

***Abstract*—Rotation equivariance constitutes one of the most general and crucial structural priors for visual data, yet it remains notably absent from current Mamba-based vision architectures. Despite the success of Mamba in natural language processing and its growing adoption in computer vision, existing visual Mamba models fail to account for rotational symmetry in their design. This omission renders them inherently sensitive to image rotations, thereby constraining their robustness and cross-task generalization. To address this limitation, we incorporate rotation symmetry, a universal and fundamental geometric prior in images, into Mamba-based architectures. Specifically, we introduce EQ-VMamba, the first rotation equivariant visual Mamba architecture for vision tasks. The core components of EQ-VMamba include a carefully designed rotation equivariant cross-scan strategy and group Mamba blocks. Moreover, we provide a rigorous theoretical analysis of the intrinsic equivariance error, demonstrating that the proposed architecture enforces end-to-end rotation equivariance throughout the network. Extensive experiments across multiple benchmarks—including high-level image classification, mid-level semantic segmentation, and low-level image super-resolution—demonstrate that EQ-VMamba consistently improves rotation robustness and achieves superior or competitive performance compared to non-equivariant baselines, while requiring approximately 50% fewer parameters. These results indicate that embedding rotation equivariance not only effectively bolsters the robustness of visual Mamba models against rotation transformations, but also enhances overall performance with significantly improved parameter efficiency. Code is available at https://github.com/zhongchenzhao/EQ-VMamba.**

***Index Terms*—Rotation equivariant Mamba, equivariant networks, visual Mamba, state space models.**

I. Introduction

In recent years, Mamba [1] has emerged as one of the most promising next-generation foundational architectures in deep learning, succeeding convolutional neural networks (CNNs) [2]–[6] and Transformers [7]–[9]. Unlike Transformers, which suffer from quadratic computational complexity with respect to input length, Mamba builds upon the core paradigm of State Space Models (SSMs) [10]–[12] and introduces an interpretable selective scan mechanism to model long-range dependencies, establishing itself as the first linear-complexity architecture to achieve performance comparable to Transformers in natural language processing (NLP).

Following Mamba's success in NLP, numerous studies [13]–[17] have explored its adaptation to the visual domain. For instance, Vim [13] directly replaces the self-attention mechanism in Vision Transformers (ViTs) with a bidirectional Mamba block, providing the first validation of Mamba's feasibility for vision applications. To better accommodate the structural discrepancy between 2D image tokens and 1D textual sequences, VMamba [14] introduces a Visual State-Space (VSS) block with a cross-scan strategy, enabling each token to symmetrically integrate global information from four directions in the 2D plane. As a result, VMamba surpasses many Transformer-based networks, including the representative Swin Transformer [9], on high-level vision tasks, highlighting the potential of Mamba-based architectures for visual recognition. Subsequently, MambaIR [17] extends this cross-scan strategy to low-level vision tasks, proposing the first Mamba-based model for image restoration and achieving comparable or superior results to state-of-the-art Transformer-based models.

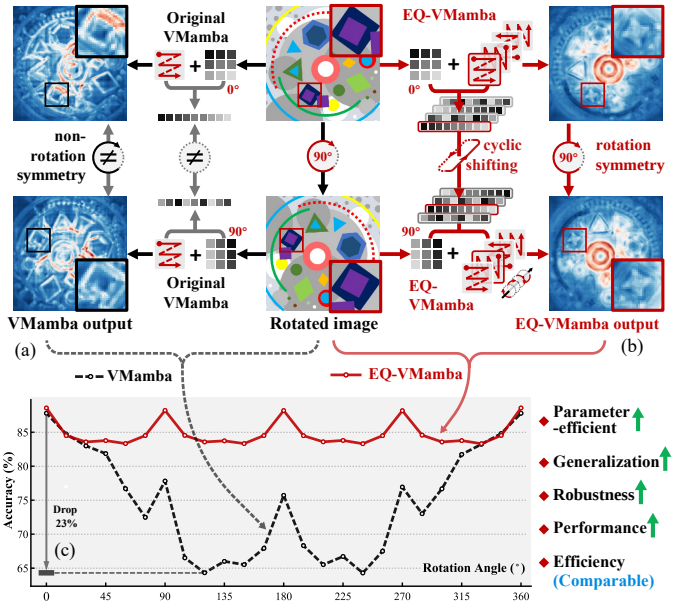

Fig. 1. (a)-(b) Visualization of output feature maps for an input image and its rotated version using VMamba and our proposed EQ-VMamba, respectively. (c) Performance comparison between VMamba and EQ-VMamba on the rotated ImageNet-100 dataset.

Despite these advances, directly adapting Mamba from NLP to vision remains far from fully exploiting its potential, due to the fundamental cross-modal discrepancies. Existing studies, represented by VMamba [14], have primarily focused on bridging the structural gaps between images and language, such as the mismatch between 1D sequences and 2D spatial layouts. However, they largely overlook another critical issue: the discrepancies in intrinsic content properties. Specifically, unlike textual data, natural images exhibit pronounced geometric symmetries: identical or similar patterns recur across various positions, orientations, and scales within an image [18]. Neglecting these symmetries inherently limits the design effi-

Zhongchen Zhao, Qi Xie, Keyu Huang, Deyu Meng, and Zongben Xu are with the School of Mathematics and Statistics, Xi'an Jiaotong University, Shaanxi, P.R. China (e-mail: zhongchenzhao@stu.xjtu.edu.cn, xie.qi@mail.xjtu.edu.cn, keyuhuang@stu.xjtu.edu.cn, dymeng@mail.xjtu.edu.cn, zbxu@mail.xjtu.edu.cn).

Lei Zhang is with the Department of Computing, the Hong Kong Polytechnic University, Hong Kong, P.R. China (e-mail: cslzhang@comp.polyu.edu.hk).

ciency of Mamba-based vision models, hindering the pursuit of more parameter-efficient architectures.

In recent years, incorporating geometric symmetry priors into neural networks has been established as an effective approach to enhance generalization and robustness [19]–[34]. Formally, prior works [19], [20] have formalized such priors as the requirement of equivariance: a model's prediction for a transformed image (e.g., translated, rotated, or reflected) should be consistent with the transformation applied to the prediction for the original image. Fundamental architectures such as CNNs and ViTs inherently possess certain equivariant properties. For instance, CNNs explicitly embed translation equivariance through weight sharing in sliding convolution kernels; rotation equivariant CNNs [19], [20] further extend this by sharing kernels across an additional group dimension, thereby reducing the number of parameters while improving generalization. Similarly, recent studies [23]–[25], [31], [32], [35] reveal that the self-attention mechanism in ViTs exhibits inherent translation, rotation, and reflection equivariances, enabling these models to avoid interference from redundant spatial transformations and efficiently extract semantically meaningful features.

In contrast to CNNs and ViTs, VMamba inherently lacks rotation equivariance. This limitation primarily stems from its core Visual State-Space (VSS) block, which exhibits weaker rotation equivariance than the convolution operators in CNNs and the self-attention mechanism in ViTs. Specifically, although the VSS block employs a four-way scanning mechanism to traverse 2D image tokens, rotational transformations of the input image still undesirably alter the scanning order, rendering the model highly sensitive to such transformations at the global level. Moreover, unlike learnable operators in CNNs and ViTs, which can approximate or even achieve rotation equivariance through gradient-based optimization, the predefined and fixed scanning mechanism in VMamba fundamentally prevents the model from learning rotation equivariant representations. Furthermore, the rotational symmetry of local structures is also disrupted during the tokenization process and the feature modeling within VSS blocks.

This inherent lack of equivariance, spanning both global and local levels, results in poor robustness of VMamba against rotational perturbations across high-level, mid-level, and low-level vision tasks. As illustrated in Fig. 1, when the same image is presented at different rotation angles, VMamba extracts different features and produces entirely different outputs (Fig. 1(a)), leading to significant performance degradation on both image classification (Fig. 1(c)) and semantic segmentation (Table III). These observations underscore the importance of developing a rotation equivariant VMamba to enhance the model's generalization, robustness, and parameter efficiency.

However, designing a strictly rotation equivariant VMamba presents several non-trivial challenges. To guarantee end-to-end rotation equivariance, each module within the architecture must individually satisfy the equivariance constraint. This imposes three key requirements: 1) a redesigned rotation equivariant scanning mechanism for 2D images; 2) a reformulation of the Mamba block to preserve equivariance throughout the state-space transformation; 3) the adaptation of other non-equivariant modules (e.g., the patch embedding layer and task-specific decoders) to rotation equivariant counterparts.

Recently, Spectral VMamba [34] has also recognized the critical importance of rotation robustness for VMamba. However, it offers only a compromised solution by constructing a rotation invariant model rather than a fully equivariant one. Notably, achieving invariance requires only orientation-agnostic local feature extraction, which is considerably simpler than achieving equivariance, where directional information must be preserved throughout the network. Moreover, discarding the directional information of local features inevitably leads to significant performance degradation, as will be demonstrated in our subsequent experiments.

In this paper, we propose EQ-VMamba, a strictly 90-degree rotation equivariant visual Mamba architecture that effectively alleviates the poor robustness of VMamba to image rotations. To the best of our knowledge, this is the first work to extend rotation equivariant design principles from CNN- and Transformer-based architectures to the emerging Mamba-based architecture, thereby enriching the existing framework of equivariant neural networks. The main contributions of this paper can be summarized as follows:

- **Model Architecture:** We present the first rigorous formulation for designing a 90-degree rotation equivariant Mamba architecture. Specifically, we propose a rotation equivariant cross-scan (EQ-cross-scan) strategy with four rotationally symmetric scanning paths. Furthermore, we reformulate the Mamba block to construct the rotation equivariant group Mamba blocks. Building on these designs, we construct an equivariant Visual State-Space (EQ-VSS) block and adapt two representative models, VMamba for high/mid-level and MambaIR for low-level vision tasks, into their equivariant counterparts: EQ-VMamba and EQ-MambaIR.
- **Parameter Efficiency:** Through careful architectural design, EQ-VMamba maintains a computational complexity comparable to its non-equivariant counterparts. Moreover, by sharing parameters across the group dimension, our approach reduces the total number of learnable parameters by approximately 50% (as shown in Table I), significantly enhancing parameter utilization efficiency.
- **Theoretical Analysis:** We provide a comprehensive theoretical foundation for the proposed EQ-VMamba architecture. Through the equivariance error analysis, we prove that the EQ-cross-scan/merge, the group Mamba blocks, and the overall EQ-VMamba architecture all achieve zero equivariance error under 90-degree rotations.
- **Empirical Validation:** Extensive experiments across high-level image classification, mid-level semantic segmentation, and low-level super-resolution tasks demonstrate that EQ-VMamba and EQ-MambaIR consistently outperform their non-equivariant counterparts, while using fewer parameters. Evaluations on rotated benchmarks confirm that EQ-VMamba effectively alleviates the rotational robustness limitations of visual Mamba. Collectively, these results demonstrate that incorporating rotation equivariance into the Mamba framework not only significantly enhances robustness against rotation

transformations but also improves overall performance.

The remainder of this paper is organized as follows. Sec. II reviews related work. Sec. III details the proposed rotation equivariant visual Mamba, together with theoretical analyses of its equivariance error. Sec. IV presents extensive experimental results across multiple vision tasks. Finally, Sec. V concludes the paper and discusses future research directions.

II. Related Work

A. Visual Mamba

As the dominant foundational architecture in deep learning, the Transformer [7] is primarily constrained by the quadratic complexity of its self-attention mechanism, which scales quadratically with input sequence length. This computational bottleneck severely restricts its efficiency when modeling long-range dependencies. In recent years, numerous sub-quadratic architectures have been proposed to mitigate this limitation, including linear attention [36], sparse Transformers [37], and various recurrent neural networks [38]–[40]. However, these alternatives generally struggle to strike an optimal balance between computational efficiency and modeling capacity.

Recently, Mamba [1], a representative state space model (SSM), has for the first time achieved Transformer-level performance on NLP tasks while maintaining linear-time complexity, marking a significant milestone in efficient sequence modeling. Specifically, Mamba inherits the recurrent propagation mechanism of SSMs [10]–[12] for linear-time sequence modeling, and further introduces a powerful input-dependent selective scan mechanism, allowing the model to selectively propagate or forget historical information along the scanning sequence. Owing to its efficiency and efficacy, Mamba has rapidly emerged as a promising alternative to Transformers, attracting considerable attention from the research community.

Inspired by Mamba's success in NLP, numerous studies [13]–[16], [41]–[43] have explored its applicability to vision tasks. Vim [13] pioneered this by replacing the original unidirectional scanning strategy with a bidirectional counterpart tailored for images. Subsequently, VMamba [14] observed that the 1D scanning strategy originally designed for text sequences in Mamba is ill-suited to the 2D structure of images and proposed a cross-scan strategy (i.e., a four-way scanning mechanism) to integrate contextual global information from four directions. Coupled with a series of architectural refinements, VMamba achieves superior performance on high-level vision tasks, surpassing Swin Transformer [9] in both accuracy and inference throughput.

Beyond high-level vision tasks, Mamba has been extended to a broader range of visual domains, including image restoration [17], [44], [45], image generation [46], video analysis [47], remote sensing images [48], [49], point cloud analysis [50], [51], and medical image analysis [52]. Among these, MambaIR [17] introduced the first Mamba-based framework for image restoration, leveraging the cross-scan strategy of VMamba to enhance local features with a global receptive field while incorporating channel attention mechanisms to mitigate channel redundancy. Extensive experiments on various image restoration benchmarks demonstrate that MambaIR achieves competitive or superior performance compared to many well-established CNN- and Transformer-based methods [53], [54].

Although the significant potential of Mamba-based architectures in the visual domain has been demonstrated, visual Mamba still suffers from an evident limitation: poor robustness to rotation transformations of input images. To address this deficiency, we develop EQ-VMamba by explicitly embedding rotation equivariance into the Mamba architecture.

B. Rotation Equivariant Neural Networks

Incorporating rotation symmetry priors into neural networks has long been an important research direction in deep learning. Over the past few years, numerous studies [19]–[34] have attempted to explicitly or implicitly incorporate the rotation symmetry prior into various network architectures. Early efforts [27], [29], [55], [56] primarily relied on data augmentation [57] and regularization to implicitly enforce rotation equivariance. However, these methods lack formal theoretical guarantees and often exhibit unstable performance in preserving strict equivariance [32].

Recent works [19]–[22], [30], [32], [58], [59] have focused more on the principled design of rotation equivariant neural networks that explicitly embed rotation equivariance. For example, G-CNN [19] was the first to successfully establish the group-equivariant convolutional framework, achieving $\pi/2$ rotation equivariance with rigorous theoretical guarantees. Building on group convolution, SFCNNs [30] and E2-CNN [20] utilized the filter parametrization techniques for arbitrary-degree equivariance in the continuous domain. Subsequently, PDO-eConvs [21] and PDO-eS2CNNs [59] introduced the first equivariance error analysis for group equivariant convolutions, providing rigorous theoretical underpinnings. Furthermore, F-Conv [22] leveraged Fourier series expansion to construct high-accuracy filter-parameterized equivariant convolutions, achieving evidently better performance than classical non-equivariant CNNs on image super-resolution tasks.

Beyond convolutional architectures, B-Conv [32] introduced a rotation equivariant linear layer for multilayer perceptrons (MLPs) and constructed a rotation equivariant implicit neural representation framework for arbitrary-scale image super-resolution. For Transformer-based architectures, several studies [23]–[25], [31], [32], [35] have revealed that the core self-attention mechanism in ViTs possesses inherent rotational properties, leading to the design of equivariant ViTs.

Despite these advances across CNNs and Transformers, research on rotation equivariant Mamba-based architectures remains largely unexplored. The recent Spectral VMamba [34] represents an initial attempt, employing a rotation invariant scanning strategy derived from spectral decomposition. However, due to the absence of a rotational group dimension, this approach achieves only rotation *invariance* rather than *equivariance*, thereby discarding essential directional information of local features and limiting its applicability to mid-level and low-level vision tasks. Moreover, the reliance on spectral decomposition introduces considerable computational overhead. In contrast, our proposed EQ-VMamba is a group-based equivariant architecture that preserves the orientation

information of local features. Moreover, the proposed EQ-cross-scan strategy is simple and efficient, ensuring strict symmetry without incurring additional computational cost.

III. Rotation Equivariant Visual Mamba

In this section, we present a principled framework for designing EQ-VMamba, a Mamba-based architecture with strict rotation equivariance under the p4 group (i.e., $\{0°, 90°, 180°, 270°\}$). Beyond the p4 rotation group, our formulation is inherently extensible to finer geometric transformations, such as p8 rotation and reflection groups, providing a generalized foundation for equivariant state-space modeling.

The remainder of this section is organized as follows. First, we establish the necessary preliminaries regarding the formulation of the Mamba architecture and the formal definition of rotation equivariance. Second, we provide a detailed exposition of the EQ-VMamba architecture, including: 1) the overall architecture; 2) the design of equivariant modules, including the EQ-patch embedding, the EQ-cross-scan/merge strategy, and EQ-VSS blocks; 3) a rigorous theoretical equivariance analysis for both the proposed individual modules and the entire network. Finally, we introduce two representative Mamba-based instantiations, EQ-VMamba and EQ-MambaIR, to demonstrate the framework's versatility across high-level, mid-level, and low-level vision tasks.

A. Preliminaries

Formulation of Mamba. Mamba [1] extends structured state space sequence models (S4) [11] by introducing a selective mechanism into the recurrent state propagation. Specifically, Mamba maps an input sequence $\boldsymbol{x} \in \mathbb{R}^{L}$[1] to an output sequence $\boldsymbol{y} \in \mathbb{R}^{L}$ by maintaining a hidden state $\boldsymbol{h}_i \in \mathbb{R}^{N}$, which is updated via an input-dependent state transition matrix $\boldsymbol{A}_i \in \mathbb{R}^{N\times N}$ as follows:

$$\begin{aligned} \boldsymbol{h}_i &= \boldsymbol{A}_i \boldsymbol{h}_{i-1} + \boldsymbol{B}_i x_i, \\ y_i &= \boldsymbol{C}_i^{\top} \boldsymbol{h}_i + D x_i, \end{aligned} \tag{1}$$

where $\boldsymbol{A}_i$ is a diagonal matrix with elements bounded in $(0, 1]$, $\boldsymbol{B}_i, \boldsymbol{C}_i \in \mathbb{R}^{N}$ are input-dependent parameters generated by linear projections, and $D \in \mathbb{R}$ denotes a skip-connection coefficient. Here, L and N represent the sequence length and hidden state dimension, respectively. The selective nature of $\boldsymbol{A}_i$ enables the model to dynamically propagate or forget historical information, significantly enhancing its capability for long-range dependency modeling.

Definition of Rotation Equivariance. Rotation equivariance requires that applying a rotation transformation to the input induces a predictable, corresponding transformation of the output, thereby preserving the structural relationship between features. Formally, let Ψ be a mapping from an input space to an output space, and $\mathcal{G}$ be a group of rotation transformations defined as $\mathcal{G} = \{G_t | t = 1, 2, \cdots, T\}$, where

$$G_t = \begin{bmatrix} \cos 2\pi(t-1)/T & \sin 2\pi(t-1)/T \\ -\sin 2\pi(t-1)/T & \cos 2\pi(t-1)/T \end{bmatrix}. \tag{2}$$

[1]For a multi-channel input sequence $\boldsymbol{x} \in \mathbb{R}^{L\times C}$, Mamba processes each channel independently and in parallel.

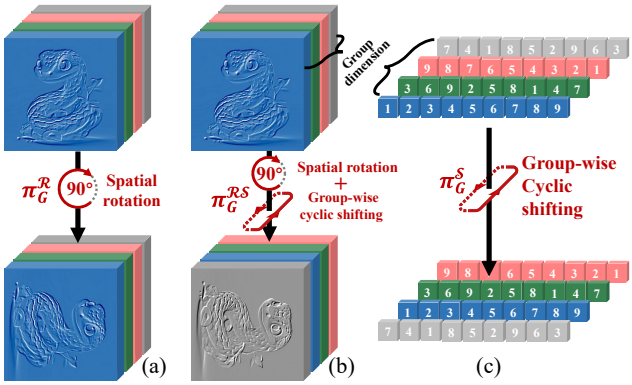

Fig. 2. Illustration of the group dimension (indexed by colors), and three fundamental transformation operators utilized in our equivariant framework. (a)-(c) illustrate $\pi_G^{\mathcal{R}}(\cdot)$, $\pi_G^{\mathcal{R}S}(\cdot)$, and $\pi_G^{\mathcal{S}}(\cdot)$, respectively.

The mapping $\Psi(\cdot)$ is equivariant with respect to $\mathcal{G}$ if, for any rotation matrix $G \in \mathcal{G}$, it satisfies:

$$\Psi\left(\pi_G^{\mathcal{R}}\left(\boldsymbol{I}\right)\right) = \tilde{\pi}_G^{\mathcal{R}}\left(\Psi\left(\boldsymbol{I}\right)\right), \tag{3}$$

where $\pi_G^{\mathcal{R}}(\cdot)$ denotes the spatial rotation transformation G acting on the input $\boldsymbol{I}$, and $\tilde{\pi}_G^{\mathcal{R}}(\cdot)$ denotes the induced transformation on the output $\Psi(\boldsymbol{I})$.

Group Dimension and Transformations.

As illustrated in Fig. 2, in group-based equivariant networks, the feature map typically incorporates an additional dimension, namely the group dimension. Specifically, whereas feature maps in conventional networks have the shape $H \times W \times \hat{C}$ (where H, W, and $\hat{C}$ denote the height, width, and number of channels, respectively), those in group-based equivariant networks are of shape $H \times W \times C \times T$, where $T = |\mathcal{G}|$ is the number of elements in the group and C is typically set to $\frac{\hat{C}}{T}$ to maintain computational parity. As will become evident in the subsequent sections, this additional group dimension plays a crucial role in preserving directional information and enabling the construction of equivariant networks. Following the notation of [21], for a feature map $\boldsymbol{X} \in \mathbb{R}^{H\times W\times C\times T}$, we denote its group component corresponding to $G \in \mathcal{G}$ as $\boldsymbol{X}^G \in \mathbb{R}^{H\times W\times C}$, where G serves both as a rotation matrix and as an index along the group dimension.

While rotation transformations on images are intuitively straightforward, on feature maps equipped with a group dimension, spatial rotation becomes coupled with a cyclic shifting along the group dimension. Specifically, in this paper, our framework primarily involves three types of transformations:

(I) $\pi_G^{\mathcal{R}}(\cdot)$: rotation in the spatial domain without altering the group dimension. As shown in Fig. 2(a), this transformation is typically applied to input images.

(II) $\pi_G^{\mathcal{R}S}(\cdot)$: rotation in the spatial domain combined with a cyclic shifting along the group dimension, as shown in Fig. 2(b). Formally, for any feature map $\boldsymbol{X} \in \mathbb{R}^{H\times W\times C\times T}$, we have:

$$\left(\pi_{\hat{G}}^{\mathcal{R}S}(\boldsymbol{X})\right)^{G} = \pi_{\hat{G}}^{\mathcal{R}}\left(\boldsymbol{X}^{\hat{G}^{-1}G}\right), \quad \forall G, \hat{G} \in \mathcal{G}. \tag{4}$$

This transformation is particularly common in prior equivariant CNNs and is typically applied to feature maps that carry a group dimension.

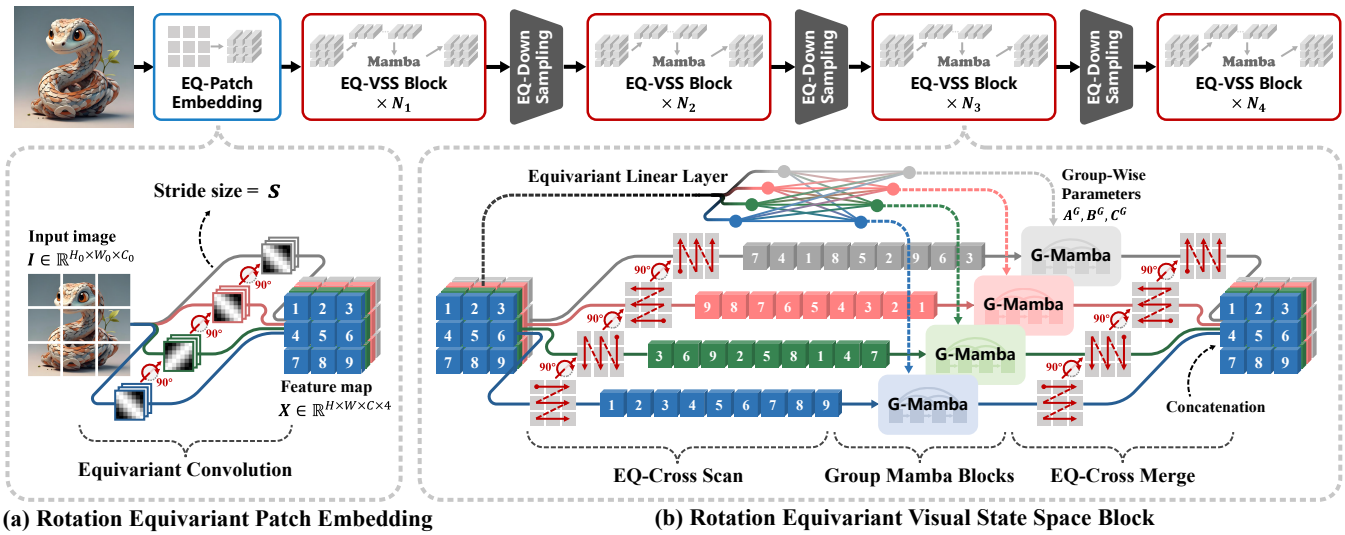

(a) Rotation Equivariant Patch Embedding **(b) Rotation Equivariant Visual State Space Block**

Fig. 3. Overall architecture of the proposed end-to-end rotation equivariant visual Mamba (EQ-VMamba). The framework mainly comprises: (a) an EQ-patch embedding module that tokenizes the input image into group-structured feature maps, and (b) a stack of EQ-VSS blocks for hierarchical feature extraction. Each EQ-VSS block integrates an EQ-cross-scan operation for image-to-sequence flattening, group Mamba blocks for sequence modeling, and an EQ-cross-merge operation for sequence-to-image reconstruction.

(III) $\pi_G^S(\cdot)$: cyclic shifting along the group dimension, with no change in the spatial domain. As shown in Fig. 2(c), for a feature map $\boldsymbol{X}$, we have

$$(\pi_{\hat{G}}^S(\boldsymbol{X}))^G = \boldsymbol{X}^{\hat{G}^{-1}G}, \quad \forall G, \hat{G} \in \mathcal{G}. \tag{5}$$

This transformation is applied to the scanning order of Mamba in our proposed framework.

Throughout this paper, we focus on the design of EQ-VMamba under the 90-degree rotation group (i.e., the p4 group), corresponding to $T = 4$.

B. Overall Architecture of EQ-VMamba

To construct an end-to-end rotation equivariant visual Mamba architecture, each constituent module must strictly satisfy the equivariance constraint defined in Eq. (3). Driven by this requirement, we adopt VMamba [14]—one of the most representative visual Mamba backbones—as our baseline, and systematically reformulate all non-equivariant components into their rotation equivariant counterparts, yielding the proposed EQ-VMamba architecture. The overall architecture of the EQ-VMamba backbone is illustrated in Fig. 3. Specifically, it consists of the following key equivariant modules.

Rotation Equivariant Patch Embedding. The vanilla VMamba begins with a patch embedding layer that partitions the input image into patches and tokenizes them into an initial feature map. However, this standard patch embedding module lacks rotation equivariance. To address this, we develop a rotation equivariant patch embedding that explicitly encodes the orientation information of each patch into the rotation group dimension of the feature map.

Rotation Equivariant Visual State-Space Block. Following patch embedding, VMamba utilizes a stack of multiple Visual State-Space (VSS) blocks for hierarchical feature extraction. Each standard VSS block consists of three stages: 1) flattening the 2D feature map into four 1D sequences via the cross-scan mechanism; 2) processing these sequences with

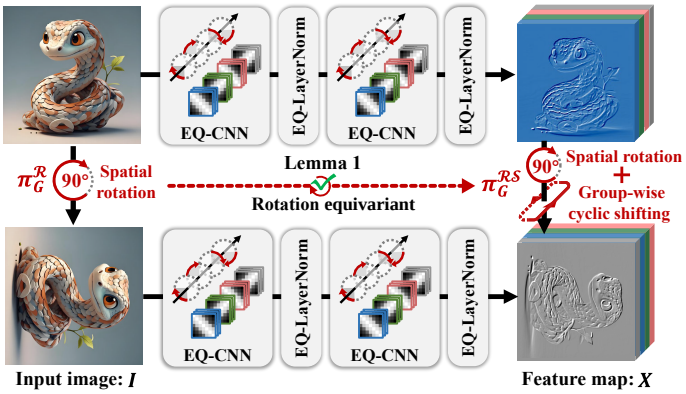

Fig. 4. Illustration of the rotation equivariant patch embedding. A spatial rotation applied to the input image induces a joint transformation on the output feature map, i.e., $\mathrm{PE}_{eq}(\pi_G^{\mathcal{R}}(\boldsymbol{I})) = \pi_G^{\mathcal{RS}}(\mathrm{PE}_{eq}(\boldsymbol{I}))$.

four independent Mamba blocks; and 3) reconstructing the 2D feature map from output sequences via cross-merge (i.e., the inverse operation of cross-scan). However, both the cross-scan/merge operations and the independently parameterized Mamba blocks lack rotation equivariance. To address this, we first propose rotation equivariant cross-scan/merge to ensure equivariance during the flattening and reconstruction stages. Furthermore, we introduce the group Mamba blocks to ensure rotation equivariance during the sequence modeling stage. By integrating these components, we construct a rotation equivariant EQ-VSS block.

Beyond the patch embedding and EQ-VSS blocks, other essential components within VMamba—such as depthwise convolution and down/up-sampling—also require equivariant modifications to ensure rotation equivariance throughout the network. Fortunately, rotation equivariant counterparts of these modules are readily available [20] and can be directly incorporated into the architecture. By replacing all non-equivariant components with their equivariant counterparts, we obtain an end-to-end rotation equivariant Mamba-based architecture that maintains the original Mamba's efficiency while significantly

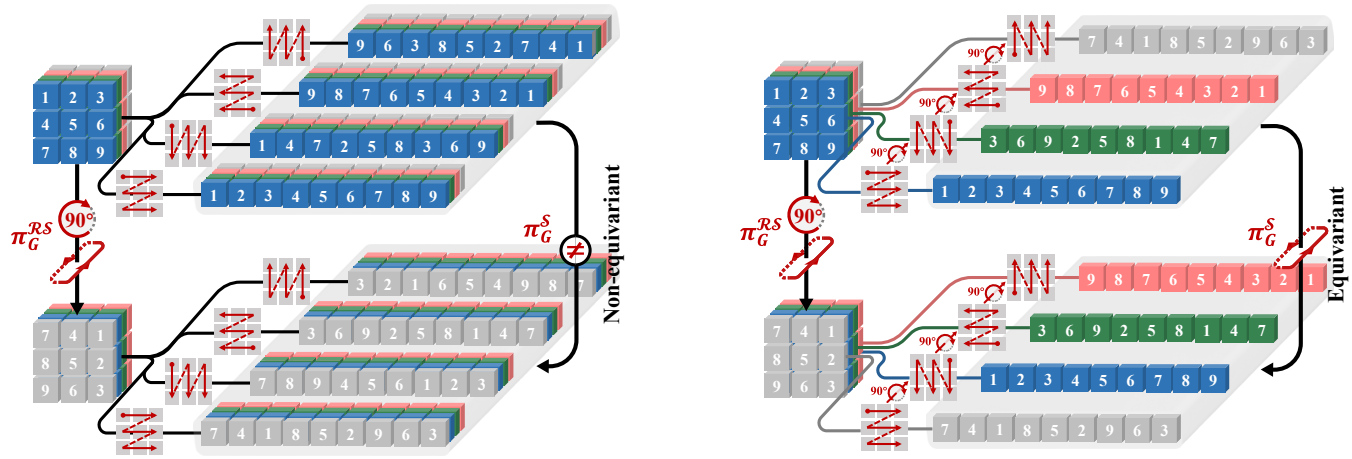

(a) Cross-scan (VMamba) (b) EQ-cross-scan (EQ-VMamba)

Fig. 5. Comparison between the non-equivariant cross-scan and the proposed equivariant EQ-cross-scan. (a) Under a 90° rotation of the input image, the standard cross-scan in VMamba fails to maintain sequence consistency. (b) In contrast, EQ-cross-scan preserves the ordering of tokens within each 1D sequence, ensuring rigorous structural correspondence between the rotated and unrotated representations.

enhancing its robustness to rotation transformations.

C. Design of Rotation Equivariant Patch Embedding

The vanilla patch embedding in VMamba performs tokenization using overlapping strided convolutional layers followed by LayerNorm2d. However, this standard patch embedding is not rotation equivariant and fails to preserve the orientation information of input image patches.

To overcome this limitation, we develop a rotation equivariant patch embedding (EQ-patch embedding) by replacing the standard convolutional layers with rotation equivariant CNN (EQ-CNN) layers [21], [22], [30]. As illustrated in Fig. 4, the EQ-CNN layer $\Psi(\cdot)$ achieves rotation equivariance by sharing a base kernel $\boldsymbol{W}_\Psi$ across discrete rotations within a defined group. Formally, given an input image $\boldsymbol{I} \in \mathbb{R}^{H_0 \times W_0 \times C_0}$, the EQ-CNN layer $\Psi(\cdot)$ maps it to a group-structured feature map $\hat{X} \in \mathbb{R}^{\frac{H_0}{s} \times \frac{W_0}{s} \times C \times 4}$ as follows:

$$\hat{X} = \Psi(\boldsymbol{I}), \text{ with } \hat{X}^G = \pi_G^{\mathcal{R}}(\boldsymbol{W}_\Psi) * \boldsymbol{I} + \boldsymbol{b}_\Psi, \ \forall G \in \mathcal{G}, \quad (6)$$

where $*$ denotes the convolution operation, s is the stride step, C is the output channel number, and $\boldsymbol{W}_\Psi \in \mathbb{R}^{K \times K \times C_0 \times C}$ and $\boldsymbol{b}_\Psi \in \mathbb{R}^C$ denote the learnable weights and biases, respectively.

By stacking multiple EQ-CNN layers (typically two layers with a stride of 2) and EQ-LayerNorm layers [20], we construct an equivariant EQ-patch embedding block $\mathrm{PE}_{eq}(\cdot)$ that maps an input image to a group-structured feature map:

$$\boldsymbol{X} = \mathrm{PE}_{eq}(\boldsymbol{I}). \quad (7)$$

Based on this formulation, we have the following lemma [22].

Lemma 1. *Let $\boldsymbol{I} \in \mathbb{R}^{H_0 \times W_0 \times C_0}$ be an input image and let $\mathrm{PE}_{eq}(\cdot)$ denote the EQ-patch embedding defined in (7). For any group element $G \in \mathcal{G}$, the following equivariance property holds:*

$$\mathrm{PE}_{eq}\left(\pi_G^{\mathcal{R}}(\boldsymbol{I})\right) = \pi_G^{\mathcal{RS}}\left(\mathrm{PE}_{eq}(\boldsymbol{I})\right). \quad (8)$$

Lemma 1 indicates that a spatial rotation applied to the input image induces a corresponding spatial rotation together with a cyclic shifting across the rotation group dimension in the output feature map.

D. Design of Rotation Equivariant Visual State-Space Block

The core contribution of EQ-VMamba is the design of a rotation equivariant Visual State-Space (EQ-VSS) block, which primarily incorporates a novel rotation equivariant cross-scan/merge strategy and group Mamba blocks.

Rotation Equivariant Cross-Scan/Merge. As formulated in Eq. (1), Mamba is inherently designed for processing one-dimensional sequential data. To apply this mechanism to 2D image data, VMamba employs a four-way cross-scan strategy that flattens 2D image tokens into four distinct 1D sequences. However, this vanilla cross-scan strategy fails to satisfy rotation equivariance. As illustrated in Fig. 5 (a), rotating the input image induces inconsistent and misaligned transformations on the resulting sequences.

To achieve rigorous equivariance, we propose a simple yet effective rotation equivariant cross-scan (EQ-cross-scan) strategy for image-to-sequence flattening. As illustrated in Fig. 5 (b), EQ-cross-scan employs four rotationally symmetric scanning paths, each independently processing one component of the feature map along the group dimension. Formally, given a group-structured 2D feature map $\boldsymbol{X} \in \mathbb{R}^{H \times W \times C \times 4}$, we define:

$$\boldsymbol{x} = \tau_{eq}(\boldsymbol{X}), \text{ with } \boldsymbol{x}^G = \tau\left(\pi_{G^{-1}}^{\mathcal{R}}\left(\boldsymbol{X}^G\right)\right), \ \forall G \in \mathcal{G}, \quad (9)$$

where $\boldsymbol{x} \in \mathbb{R}^{HW \times C \times 4}$ denotes the resulting 1D feature sequences, and $\tau(\cdot)$ represents the base scanning path (corresponding to the standard matrix-to-vector unfolding).

Symmetrically, we define the inverse operation of $\tau_{eq}(\cdot)$, termed EQ-cross-merge $\tau_{eq}^{inv}(\cdot)$ for equivariant sequence-to-image reconstruction:

$$\hat{X} = \tau_{eq}^{inv}(\boldsymbol{x}), \text{ with } \hat{X}^G = \pi_G^{\mathcal{R}}\left(\tau^{inv}\left(\boldsymbol{x}^G\right)\right), \ \forall G \in \mathcal{G}, \quad (10)$$

where $\tau^{inv}(\cdot)$ denotes the standard vector-to-matrix folding.

Based on this formulation, we establish the following theoretical guarantees (detailed proofs are provided in the supplementary material).

Theorem 1. *Let $\boldsymbol{X} \in \mathbb{R}^{H \times W \times C \times 4}$ be a group-structured feature map and let $\boldsymbol{x} \in \mathbb{R}^{HW \times C \times 4}$ be a group-structured*

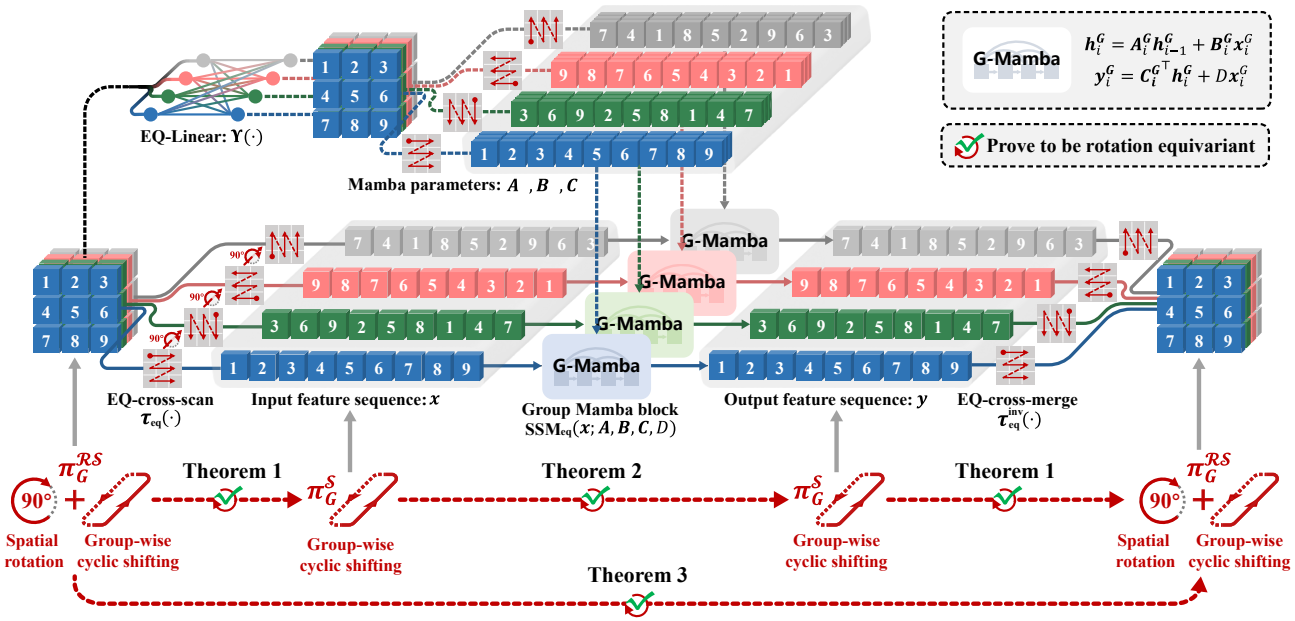

Fig. 6. **Upper**: Architectural pipeline of the proposed equivariant Visual State-Space (EQ-VSS) block. (1) The block first employs EQ-Linear layers to generate input-dependent Mamba parameters $\boldsymbol{A}$, $\boldsymbol{B}$, and $\boldsymbol{C}$. (2) These parameters, along with the input feature map, are partitioned along the group dimension and flattened into four 1D sequences via EQ-cross-scan. (3) Each feature sequence is processed in parallel by the group Mamba block using its corresponding group-wise parameters. (4) Finally, the output feature map is restored through the EQ-cross-merge operation. **Bottom**: Illustration of the proposed theoretical results, which show the correspondence between each theorem and its respective network module.

feature sequence. Let $\tau_{eq}(\cdot)$ and $\tau_{eq}^{inv}(\cdot)$ denote the EQ-cross-scan and EQ-cross-merge operators defined in (9) *and* (10)*, respectively. For any group element $\hat{G} \in \mathcal{G}$, the following equivariance properties hold:*

$$\tau_{eq}\left(\pi_{\hat{G}}^{\mathcal{RS}}\left(\boldsymbol{X}\right)\right) = \pi_{\hat{G}}^{\mathcal{S}}\left(\tau_{eq}\left(\boldsymbol{X}\right)\right), \tag{11}$$

$$\tau_{eq}^{inv}\left(\pi_{\hat{G}}^{\mathcal{S}}\left(\boldsymbol{x}\right)\right) = \pi_{\hat{G}}^{\mathcal{RS}}\left(\tau_{eq}^{inv}\left(\boldsymbol{x}\right)\right). \tag{12}$$

Theorem 1 establishes that both the EQ-cross-scan $\tau_{eq}(\cdot)$ and EQ-cross-merge $\tau_{eq}^{inv}(\cdot)$ are strictly equivariant under discrete 90-degree rotations. An intuitive illustration is provided in Fig. 5 (b): when the input image undergoes a 90° spatial rotation and a group-wise cyclic shifting, the resulting 1D sequences generated by EQ-cross-scan differ only by the corresponding permutation along the group dimension, ensuring the equivariance of the image-to-sequence flattening process.

Group Mamba Blocks. Following the image-to-sequence flattening process, the vanilla VMamba employs four independent Mamba blocks to process each of the four feature sequences in parallel. However, under rotation transformations, the group-dimensional components of feature maps will be processed by different Mamba blocks compared to the unrotated case, producing a non-equivariant output. Consequently, the independent parameterization of the Mamba blocks in VMamba lacks rotation equivariance.

To resolve this, we construct the group Mamba blocks by restructuring the learnable parameters $\boldsymbol{A}, \boldsymbol{B}$, and $\boldsymbol{C}$ in the Mamba blocks. Specifically, as illustrated in Fig. 6, we first replace the non-equivariant linear layers with EQ-Linear layers $\Upsilon(\cdot)$, while retaining all element-wise non-linear operations from the original Mamba formulation. Furthermore, to fully exploit feature interactions along the group dimension, the parameters $\boldsymbol{A}$, $\boldsymbol{B}$, and $\boldsymbol{C}$ are generated prior to the scanning operation and subsequently flattened into one-dimensional sequences consistent with the input sequence $\boldsymbol{x}$. This design enables an equivariant reformulation while preserving the original parameter generation scheme of Mamba. We illustrate the construction using parameter $\boldsymbol{A}$ as an example:

$$\boldsymbol{A} = \tau_{eq}\left(\delta_a\left(\Upsilon_a\left(\boldsymbol{X}\right)\right)\right) \tag{13}$$

where $\boldsymbol{X} \in \mathbb{R}^{H\times W\times C\times 4}$, $\boldsymbol{A} \in \mathbb{R}^{HW\times N\times N\times C\times 4}$, $\delta_a(\cdot)$ includes the element-wise non-linear operation and the reshape/diagonal operations ($\mathbb{R}^{H\times W\times NC\times 4} \rightarrow \mathbb{R}^{H\times W\times N\times N\times C\times 4}$) from the original Mamba framework, $\tau_{eq}(\cdot)$ denotes the EQ-cross-scan operator defined in Eq. (9), and $\Upsilon_a(\cdot)$ denotes an EQ-Linear layer [32], [60] defined as

$$\left(\Upsilon_a\left(\boldsymbol{X}\right)\right)^G = \boldsymbol{X} \times \pi_G^{\mathcal{S}}(\boldsymbol{W}_a) + \boldsymbol{b}_a, \ \forall G \in \mathcal{G} \tag{14}$$

where $\boldsymbol{W}_a \in \mathbb{R}^{4C\times NC}$ and $\boldsymbol{b}_a \in \mathbb{R}^{NC}$ are learnable parameters.

Similarly, parameters $\boldsymbol{B}$ and $\boldsymbol{C}$ can be generated by

$$\boldsymbol{B} = \tau_{eq}\left(\delta_b\left(\Upsilon_b\left(\boldsymbol{X}\right)\right)\right), \ \boldsymbol{C} = \tau_{eq}\left(\delta_c\left(\Upsilon_c\left(\boldsymbol{X}\right)\right)\right), \tag{15}$$

where $\boldsymbol{B}, \boldsymbol{C} \in \mathbb{R}^{HW\times N\times 4}$, $\delta_b(\cdot)$ and $\delta_c(\cdot)$ denote the reshape operation, and $\Upsilon_b(\cdot)$ and $\Upsilon_c(\cdot)$ denote EQ-Linear layers. Then, parameters $\boldsymbol{A}, \boldsymbol{B}, \boldsymbol{C}$, together with a shared scalar parameter D, are assigned to the group Mamba blocks for sequence modeling:

$$\boldsymbol{y} = \mathrm{SSM}_{\mathrm{eq}}\left(\boldsymbol{x}; \boldsymbol{A}, \boldsymbol{B}, \boldsymbol{C}, D\right), \tag{16}$$

where $\boldsymbol{y} \in \mathbb{R}^{HW\times C\times 4}$ denotes the output sequences. The group Mamba blocks comprise four parallel Mamba blocks, each modeling its corresponding group-wise feature sequences as

$$\boldsymbol{y}^G = \mathrm{SSM}\left(\boldsymbol{x}^G; \boldsymbol{A}^G, \boldsymbol{B}^G, \boldsymbol{C}^G, D\right), \ \forall G \in \mathcal{G}, \tag{17}$$

where $\mathrm{SSM}(\cdot)$ denotes the standard Mamba formulation defined in Eq. (1). Concretely, for $k = 1, 2, \cdots, C$ and $\forall G \in \mathcal{G}$,

$$\begin{aligned} \boldsymbol{h}_{i,k}^{G} &= \boldsymbol{A}_{i,k}^{G} \boldsymbol{h}_{i-1,k}^{G} + \boldsymbol{B}_{i,k}^{G} \boldsymbol{x}_{i,k}^{G}, \\ \boldsymbol{y}_{i,k}^{G} &= \boldsymbol{C}_{i,k}^{G\top} \boldsymbol{h}_{i,k}^{G} + D \boldsymbol{x}_{i,k}^{G}. \end{aligned} \tag{18}$$

Finally, the output 2D feature map is recovered through EQ-cross-merge, i.e., $\boldsymbol{Y} = \tau_{eq}^{inv}(\boldsymbol{y})$. Based on this formulation, we establish the following theoretical guarantees.

Theorem 2. *Let $\boldsymbol{X} \in \mathbb{R}^{H \times W \times C \times 4}$ be a group-structured feature map. Given the group Mamba blocks $\mathrm{SSM}_{\mathrm{eq}}(\cdot)$ defined in* (16) *with parameters $\boldsymbol{A}$, $\boldsymbol{B}$, and $\boldsymbol{C}$ derived according to* (13) *and* (15)*, the following equivariance property holds for any $\hat{G} \in \mathcal{G}$:*

$$\begin{aligned} &\mathrm{SSM}_{\mathrm{eq}}\left(\pi_{\hat{G}}^{\mathcal{S}}(\boldsymbol{x}); \pi_{\hat{G}}^{\mathcal{S}}(\boldsymbol{A}), \pi_{\hat{G}}^{\mathcal{S}}(\boldsymbol{B}), \pi_{\hat{G}}^{\mathcal{S}}(\boldsymbol{C}), D\right) \\ &\qquad = \pi_{\hat{G}}^{\mathcal{S}}\left(\mathrm{SSM}_{\mathrm{eq}}(\boldsymbol{x}; \boldsymbol{A}, \boldsymbol{B}, \boldsymbol{C}, D)\right), \end{aligned} \tag{19}$$

Theorem 2 establishes that the proposed group Mamba blocks strictly satisfy 90-degree rotation equivariance.

Entire Formulation of EQ-VSS Block. By combining EQ-cross-scan (Eq. (9)), the group Mamba block (Eq. (16)), and EQ-cross-merge (Eq. (10)), we formulate the equivariant EQ-VSS block for an input feature map $\boldsymbol{X} \in \mathbb{R}^{H \times W \times C \times T}$ as

$$\mathrm{VSS}_{\mathrm{eq}}(\boldsymbol{X}) = \tau_{eq}^{inv}\left(\mathrm{SSM}_{\mathrm{eq}}\left(\tau_{eq}(\boldsymbol{X}); \boldsymbol{A}, \boldsymbol{B}, \boldsymbol{C}, D\right)\right). \tag{20}$$

Building on Theorems 1 and 2, we establish the rotational equivariance of the entire EQ-VSS block as follows.

Theorem 3. *Under the same conditions as Theorems 1 and 2, the EQ-VSS block defined in Eq.* (20) *satisfies the equivariance property for any $\hat{G} \in \mathcal{G}$:*

$$\mathrm{VSS}_{\mathrm{eq}}\left(\pi_{\hat{G}}^{\mathcal{RS}}(\boldsymbol{X})\right) = \pi_{\hat{G}}^{\mathcal{RS}}\left(\mathrm{VSS}_{\mathrm{eq}}(\boldsymbol{X})\right), \tag{21}$$

Fig. 6 provides an intuitive illustration: a spatial rotation combined with a group-wise cyclic shifting applied to the input feature map results in identical transformations at the output of the EQ-VSS block, thereby empirically validating the theoretical equivariance property established in Theorem 3.

Remarks. By combining Lemma 1 and Theorem 3, it follows that the entire EQ-VMamba backbone achieves end-to-end equivariance under 90-degree rotations.

Moreover, it is worth emphasizing that, in the original VMamba architecture, the linear layer used to generate $\boldsymbol{A}$, $\boldsymbol{B}$, and $\boldsymbol{C}$ contains $\hat{C} \times N\hat{C}$ parameters, where $\hat{C}$ denotes the number of feature channels in the original VMamba network. To preserve consistency in the total number of feature channels, we set the channel dimension of EQ-VMamba, C, to $\hat{C}/4$. Under this setting, the number of parameters in the equivariant linear layer is reduced to $\hat{C} \times N\hat{C}/4$, namely, 25% of that in the original VMamba. Consequently, the overall network achieves a reduction of more than 50% in total parameter count, as reported in Table I.

E. Implementation of Rotation Equivariant Visual Mamba

Leveraging the proposed equivariant modules, we transform two representative Mamba-based architectures, VMamba for high-level and mid-level vision tasks and MambaIR for low-level vision tasks, into their equivariant counterparts: EQ-VMamba and EQ-MambaIR. Beyond these instantiations, the proposed formulation can be extended to render other Mamba-based visual frameworks end-to-end rotation equivariant.

EQ-VMamba for Classification and Segmentation. For high-level and mid-level vision tasks, we first construct an EQ-VMamba backbone for feature extraction by following the basic architecture of VMamba [14]. As illustrated in Fig. 3, the EQ-VMamba backbone begins with an EQ-patch embedding module that tokenizes the input image into a group-structured feature map. Subsequently, four network stages are employed to create hierarchical representations. Each stage comprises a stack of EQ-VSS blocks, followed by an EQ-downsampling layer (except for the final stage). Furthermore, all remaining non-equivariant modules—including depthwise convolution, LayerNorm2d, and Dropout—are systematically replaced with their rotation equivariant counterparts.

For image classification, we employ a simple global average pooling layer to aggregate the final feature map into a feature vector, followed by an EQ-Linear layer serving as the classification head to produce rotation equivariant predictions. For semantic segmentation, we re-engineer the classical UPerNet [61] decoder into a rotation equivariant counterpart (EQ-UPerNet) by systematically substituting its constituent modules with EQ-CNN, EQ-Dropout, and EQ-upsampling counterparts. Following the VMamba protocol, multi-level hierarchical features extracted by the EQ-VMamba backbone are fed into the EQ-UPerNet decoder to generate pixel-wise rotation equivariant segmentation predictions. Finally, we obtain an end-to-end rotation equivariant EQ-VMamba for image classification and semantic segmentation tasks.

EQ-MambaIR for Image Restoration. For low-level vision tasks, we develop EQ-MambaIR based on the MambaIR [17] architecture. The majority of MambaIR's components, such as VSS blocks and convolutional layers, can be directly replaced with their equivariant counterparts. For the reconstruction layers, we replace the original non-equivariant PixelShuffle [62] with an EQ-PixelShuffle module to achieve equivariant upsampling. Additionally, the channel attention mechanism [63] employed in MambaIR is adapted into a rotation equivariant form by replacing its internal linear layers with EQ-Linear layers. The resulting EQ-MambaIR framework provides an end-to-end rotation equivariant solution applicable to a broad range of image restoration tasks.

IV. Experimental Results

To validate the effectiveness of the proposed framework, we conduct extensive comparative experiments on four representative vision tasks: image classification, semantic segmentation, classical image super-resolution, and lightweight image super-resolution. Beyond standard benchmarks, we further evaluate the classification and segmentation performance of VMamba and EQ-VMamba on rotated datasets to assess robustness to input rotations. We also perform equivariance verification experiments to empirically quantify the equivariance errors of EQ-VMamba and EQ-MambaIR. Additionally, we compare

TABLE I
QUANTITATIVE COMPARISON OF IMAGE CLASSIFICATION PERFORMANCE ON THE IMAGENET-100 VALIDATION SET.

Model	Arch.	#Param.	FLOPs	Top-1 (%)	Top-5 (%)	Model	Arch.	#Param.	FLOPs	Top-1 (%)	Top-5 (%)
ConvNeXt-T [6]	CNN	29M	4.5G	87.06	96.70	ConvNeXt-S [6]	CNN	50M	8.7G	87.54	96.96
DeiT-S [64]	Trans.	22M	4.6G	78.88	93.64	DeiT-B [64]	Trans.	86M	17.5G	78.14	92.60
Swin-T [9]	Trans.	29M	4.5G	87.42	97.20	Swin-S [9]	Trans.	50M	8.7G	87.26	97.46
XCiT-S24 [65]	Trans.	26M	9.2G	87.14	96.98	XCiT-M24 [65]	Trans.	84M	16.2G	87.72	97.36
Vim-T [13]	SSM	7M	1.5G	82.20	95.60	Vim-S [13]	SSM	26M	5.1G	80.24	95.00
MSVMamba-M [42]	SSM	12M	1.5G	87.56	97.76	MSVMamba-T [42]	SSM	33M	4.6G	88.44	97.92
SpectralVMamba-T [34]	SSM	21M	3.9G	87.86	97.25	SpectralVMamba-S [34]	SSM	35M	6.3G	88.09	97.08
VMamba-T [14]	SSM	30M	4.9G	87.80	97.70	VMamba-S [14]	SSM	50M	8.7G	88.32	97.82
EQ-VMamba-T	SSM	**10M**	4.9G	**88.58**	**98.14**	EQ-VMamba-S	SSM	**17M**	8.7G	**88.70**	**98.22**

the equivariant Mamba-based architecture (EQ-MambaIR) with CNN-based and ViT-based equivariant networks on image super-resolution tasks (please refer to the supplementary material). Finally, systematic ablation studies are conducted to verify the necessity of an end-to-end equivariant design and the effectiveness of the proposed group Mamba blocks.

A. Image Classification

Experimental Settings. We evaluate the classification performance of EQ-VMamba on the ImageNet-100 dataset [66], a widely used subset of ImageNet-1K [67]. ImageNet-100 consists of 100 categories, with 130K images for training and 5K images for validation. Following the training protocol of VMamba [14], all models are trained from scratch using the AdamW optimizer [68] for 300 epochs with a cosine learning rate decay schedule, a batch size of 1024, an initial learning rate of 0.001, and a weight decay of 0.05. To stabilize training, we apply exponential moving average (EMA) [69] to model parameters. During training, input images are resized to 224×224, and standard data augmentations are employed, including color jittering, random rotation, AutoAugment, random erasing, Mixup, and CutMix. Moreover, we develop EQ-VMamba at two scales: tiny (EQ-VMamba-T) and small (EQ-VMamba-S). For a fair comparison, we reproduce VMamba [14] under the same experimental settings.

Experimental Results. Table I presents the comparison results on the ImageNet-100 dataset. EQ-VMamba consistently outperforms the non-equivariant VMamba baseline while utilizing approximately $1/3$ of the parameters. Specifically, EQ-VMamba-T achieves a top-1 accuracy of **88.58**%, exceeding VMamba-T by **0.78**% with a parameter reduction from 30M to 10M. Similarly, EQ-VMamba-S achieves **88.70**% top-1 accuracy, outperforming VMamba-S by **0.38**% with a parameter reduction from 50M to 17M. Furthermore, our method outperforms the rotation invariant Spectral VMamba [34] with fewer learnable parameters. These results demonstrate that the integration of rotation equivariance serves as a powerful inductive bias, boosting performance while significantly enhancing parameter efficiency through group-wise weight sharing.

Rotated Classification Experimental Results. Fig. 7 compares the classification robustness of VMamba-T, Spectral VMamba-T, and EQ-VMamba-T under various rotation angles on ImageNet-100. The results show that VMamba exhibits pronounced sensitivity to image rotation, suffering from substantial performance degradation. While Spectral

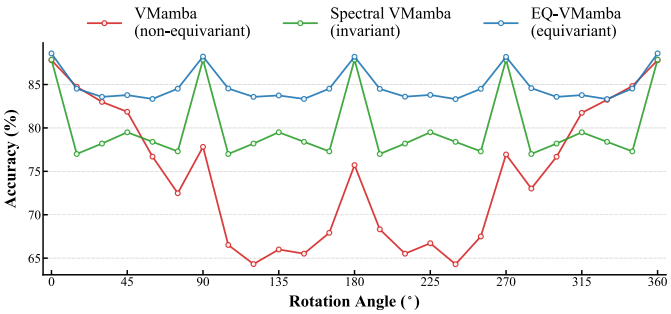

Fig. 7. Robustness comparison of VMamba-T, Spectral VMamba-T, and EQ-VMamba-T on the rotated ImageNet-100 dataset.

VMamba maintains stable performance at cardinal rotations (e.g., $0°, 90°, 180°$, and $270°$), its performance drops sharply at intermediate rotation angles. In contrast, EQ-VMamba preserves strict equivariance under 90-degree rotations and evidently demonstrates superior robustness across the entire rotation spectrum. Collectively, these results confirm that our rotation equivariant design successfully alleviates the rotational robustness limitations of VMamba.

B. Semantic Segmentation

Experimental Settings. We evaluate the semantic segmentation performance of EQ-VMamba on four widely used natural image datasets (ADE20K [70], PASCAL VOC 2012 [71], Cityscapes [72], and COCO-Stuff-164K [73]) and two remote sensing datasets (LoveDA [74] and ISPRS Potsdam [75]). All experiments are implemented using the MMSegmentation [76] framework. For Cityscapes, input images are cropped to 1024×1024 with a batch size of 8; for all other datasets, input images are cropped to 512×512 with a batch size of 16. For natural images, following prior work [34], we initialize the EQ-VMamba backbone with ImageNet-100 pretrained weights and adopt EQ-UPerNet as the decoder. All models are trained for 160K iterations using the AdamW optimizer [68] with an initial learning rate of 6×10^{-5}. For remote sensing image segmentation, following the protocol of Samba [48], models are trained from scratch for 15K iterations with an initial learning rate of 6×10^{-4}. To ensure a fair comparison, all comparison methods are reproduced under the same experimental settings.

Experimental Results. Table II summarizes the comparison results across six semantic segmentation datasets. Overall, EQ-VMamba achieves comparable performance to VMamba on natural image datasets while utilizing only approximately $1/4$ of the parameters, and substantially outperforms VMamba on

TABLE II
QUANTITATIVE COMPARISON OF **SEMANTIC SEGMENTATION** PERFORMANCE ON NATURAL/REMOTE SENSING IMAGE DATASETS (MIOU: %).

Backbone	#Param.	Natural Image				Remote Sensing Image	
		ADE20K	**VOC 2012**	**Cityscapes**	**COCO-Stuff**	**LoveDA**	**ISPRS Potsdam**
ConvNeXt-T [6]	48M	35.59	53.99	76.33	32.81	38.52	50.61
DeiT-S [64]	52M	23.13	24.17	24.29	54.23	38.74	48.63
Swin-T [9]	48M	27.05	35.73	70.05	25.83	40.78	53.78
XCiT-S24 [65]	76M	36.21	58.08	73.02	35.11	36.29	49.01
Vim-T [13]	13M	24.31	32.20	60.04	23.64	36.12	44.01
MSVMamba-M [42]	42M	37.69	59.78	78.40	35.94	41.26	55.34
VMamba-T [14]	62M	**40.15**	63.70	**78.42**	38.67	42.62	53.24
EQ-VMamba-T	**18M**	39.51	**64.46**	78.01	**38.69**	**45.69**	**59.54**
ConvNeXt-S [6]	70M	36.89	58.83	77.12	35.03	39.01	52.05
DeiT-B [64]	121M	24.43	24.85	56.26	26.40	39.21	50.71
Swin-S [9]	69M	29.19	38.89	73.43	28.20	41.23	54.69
XCiT-M24 [65]	112M	36.39	58.63	73.84	35.75	37.27	50.09
Vim-S [13]	46M	26.62	33.16	63.48	26.91	39.13	50.86
MSVMamba-T [42]	65M	40.70	65.98	78.35	36.63	43.83	57.86
VMamba-S [14]	82M	**41.68**	66.14	79.03	37.43	40.90	56.06
EQ-VMamba-S	**25M**	39.90	**66.57**	**80.36**	**38.30**	**44.04**	**62.00**

TABLE III
QUANTITATIVE COMPARISON OF **SEMANTIC SEGMENTATION** PERFORMANCE ON **ROTATED** NATURAL/REMOTE SENSING DATASETS (MIOU: %) (THE VALUES INSIDE THE PARENTHESES INDICATE THE INCREASE/DECREASE IN PERFORMANCE ON ROTATED INPUTS COMPARED WITH UNROTATED INPUTS).

Backbone	#Param.	Natural Image				Remote Sensing Image	
		ADE20K	**VOC 2012**	**Cityscapes**	**COCO-Stuff**	**LoveDA**	**ISPRS Potsdam**
VMamba-T [14]	62M	15.98 (24.17↓)	40.42 (23.28↓)	32.70 (45.72↓)	24.26 (14.41↓)	41.68 (0.94↓)	53.15 (0.09↓)
EQ-VMamba-T	**18M**	**39.59** (0.08↑)	**63.19** (1.27↓)	**78.01** (0.00)	**37.80** (0.50↓)	**45.69** (0.00)	**59.54** (0.00)
VMamba-S [14]	82M	19.60 (22.08↓)	47.54 (18.60↓)	39.42 (39.61↓)	26.51 (10.92↓)	39.19 (1.71↓)	53.08 (2.98↓)
EQ-VMamba-S	**25M**	**39.87** (0.03↓)	**65.64** (0.93↓)	**80.36** (0.00)	**37.76** (0.54↓)	**44.04** (0.00)	**62.00** (0.00)

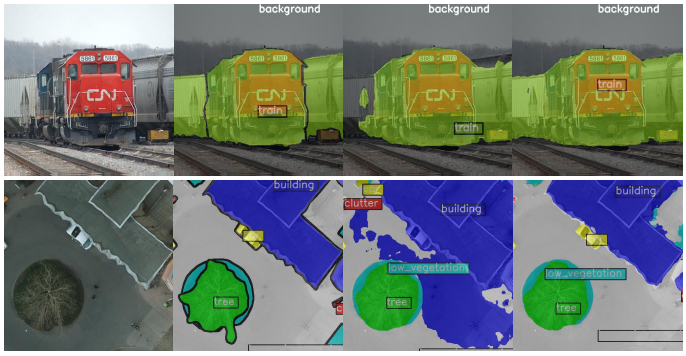

Input image Ground truth VMamba EQ-VMamba

Fig. 8. Visual comparison of segmentation results between VMamba and EQ-VMamba on the PASCAL VOC 2012 natural image dataset (top row) and the ISPRS Potsdam remote sensing dataset (bottom row).

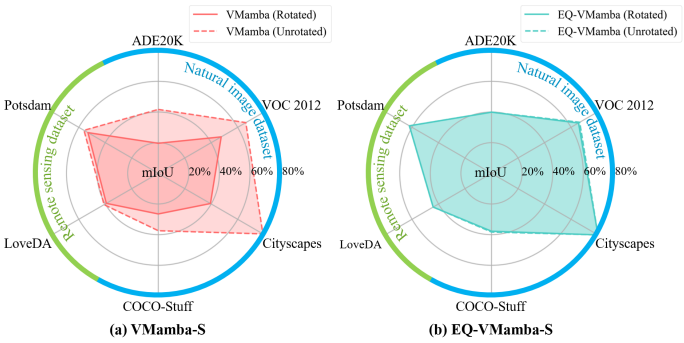

Fig. 9. Robustness comparison of VMamba and EQ-VMamba on the rotated semantic segmentation datasets. Input image rotations lead to a substantial performance degradation in VMamba, while EQ-VMamba preserves performance under 90-degree rotations.

remote sensing datasets. Specifically, on natural images, EQ-VMamba-S surpasses VMamba-S on PASCAL VOC 2012, Cityscapes, and COCO-Stuff-164K, only insignificantly behind on ADE20K. A similar trend is observed for the tiny variants, where EQ-VMamba-T outperforms VMamba-T on two of the four natural image datasets. The advantages of the proposed equivariant architecture become more pronounced on remote sensing data. Notably, EQ-VMamba-T significantly exceeds VMamba-S by **3.07**% mIoU on LoveDA and **6.30**% mIoU on ISPRS Potsdam. EQ-VMamba-S continues to exceed VMamba-S by **3.14**% mIoU on LoveDA and **5.94**% mIoU on ISPRS Potsdam. Qualitative visualizations in Fig. 8 demonstrate that EQ-VMamba generates more accurate segmentation predictions than the original VMamba in certain cases.

Rotated Segmentation Experimental Results. Table III and Fig. 9 compare the semantic segmentation robustness of VMamba and EQ-VMamba under cardinal rotations $(0°, 90°, 180°, 270°)$ across both natural and remote sensing datasets. Experimental results show that the vanilla VMamba suffers substantial performance degradation under rotation on natural images, and marginal degradation on remote sensing images. For example, VMamba-T exhibits a drastic segmen-

TABLE IV
QUANTITATIVE COMPARISON OF DIFFERENT METHODS ON THE **CLASSIC IMAGE SUPER-RESOLUTION** BENCHMARK.

Model	Scale	#Param.	**Set5**		**Set14**		**BSD100**		**Urban100**		**Manga109**	
			PSNR	SSIM	PSNR	SSIM	PSNR	SSIM	PSNR	SSIM	PSNR	SSIM
EDSR [77]	×2	42.6M	38.11	0.9602	33.92	0.9195	32.32	0.9013	32.93	0.9351	39.10	0.9773
RCAN [78]	×2	15.4M	38.27	0.9614	34.12	0.9216	32.41	0.9027	33.34	0.9384	39.44	0.9786
SAN [79]	×2	15.7M	38.31	0.9620	34.07	0.9213	32.42	0.9028	33.10	0.9370	39.32	0.9792
HAN [80]	×2	15.9M	38.27	0.9614	34.16	0.9217	32.41	0.9027	33.35	0.9385	39.46	0.9785
IPT [81]	×2	115M	38.37	-	34.43	-	32.48	-	33.76	-	-	-
SwinIR [53]	×2	11.8M	38.42	0.9623	34.46	0.9250	32.53	0.9041	33.81	0.9427	39.92	0.9797
EDT [82]	×2	11.5M	38.45	0.9624	34.57	0.9258	32.52	0.9041	33.80	0.9425	39.93	0.9800
SRFormer [54]	×2	10.4M	38.51	0.9627	34.44	0.9253	32.57	0.9046	34.09	0.9449	40.07	0.9802
MambaIR [17]	×2	20.4M	38.57	0.9627	34.67	0.9261	32.58	0.9048	34.15	0.9446	40.28	0.9806
EQ-MambaIR	×2	12.1M	**38.59**	**0.9629**	**34.76**	**0.9268**	**32.63**	**0.9056**	**34.32**	**0.9458**	**40.34**	**0.9810**
EDSR [77]	×3	42.6M	34.65	0.9280	30.52	0.8462	29.25	0.8093	28.80	0.8653	34.17	0.9476
RCAN [78]	×3	15.4M	34.74	0.9299	30.65	0.8482	29.32	0.8111	29.09	0.8702	34.44	0.9499
SAN [79]	×3	15.7M	34.75	0.9300	30.59	0.8476	29.33	0.8112	28.93	0.8671	34.30	0.9494
HAN [80]	×3	16.1M	34.75	0.9299	30.67	0.8483	29.32	0.8110	29.10	0.8705	34.48	0.9500
IPT [81]	×3	115M	34.81	-	30.85	-	29.38	-	29.49	-	-	-
SwinIR [53]	×3	11.8M	34.97	0.9318	30.93	0.8534	29.46	0.8145	29.75	0.8826	35.12	0.9537
EDT [82]	×3	11.5M	34.97	0.9316	30.89	0.8527	29.44	0.8142	29.72	0.8814	35.13	0.9534
SRFormer [54]	×3	10.6M	35.02	0.9323	30.94	0.8540	29.48	0.8156	30.04	0.8865	35.26	0.9543
MambaIR [17]	×3	20.4M	35.08	0.9323	30.99	0.8536	29.51	0.8157	29.93	0.8841	35.43	0.9546
EQ-MambaIR	×3	12.2M	**35.13**	**0.9327**	**31.08**	**0.8546**	**29.53**	**0.8170**	**30.06**	**0.8869**	**35.48**	**0.9550**
EDSR [77]	×4	43.0M	32.46	0.8968	28.80	0.7876	27.71	0.7420	26.64	0.8033	31.02	0.9148
RCAN [78]	×4	15.6M	32.63	0.9002	28.87	0.7889	27.77	0.7436	26.82	0.8087	31.22	0.9173
SAN [79]	×4	15.7M	32.64	0.9003	28.92	0.7888	27.78	0.7436	26.79	0.8068	31.18	0.9169
HAN [80]	×4	16.1M	32.64	0.9002	28.90	0.7890	27.80	0.7442	26.85	0.8094	31.42	0.9177
IPT [81]	×4	116M	32.64	-	29.01	-	27.82	-	27.26	-	-	-
SwinIR [53]	×4	11.9M	32.92	0.9044	29.09	0.7950	27.92	0.7489	27.45	0.8254	32.03	0.9260
EDT [82]	×4	11.6M	32.82	0.9031	29.09	0.7939	27.91	0.7483	27.46	0.8246	32.05	0.9254
SRFormer [54]	×4	10.5M	32.93	0.9041	29.08	0.7953	27.94	0.7502	27.68	**0.8311**	32.21	0.9271
MambaIR [17]	×4	20.4M	33.03	0.9046	29.20	0.7961	**27.98**	0.7503	27.68	0.8287	32.32	**0.9272**
EQ-MambaIR	×4	12.2M	**33.04**	**0.9047**	**29.21**	**0.7964**	**27.98**	**0.7506**	**27.70**	0.8300	**32.33**	0.9270

tation accuracy decline of **24.17%** on the rotated ADE20K dataset. In contrast, EQ-VMamba maintains nearly constant performance across all datasets, demonstrating markedly superior robustness. The negligible performance fluctuations observed on certain datasets (e.g., ADE20K) are attributed to irregular test image resolutions rather than any deficiency in architectural equivariance. Specifically, irregular input resolutions introduce subtle differences in patch partitioning after rotation, which can be mitigated by employing zero-padding to standardize input resolutions.

Analysis of Experimental Results. Experimental results in Tables II and III reveal a noteworthy phenomenon: EQ-VMamba achieves substantially larger performance gains on remote sensing datasets than natural image datasets. Correspondingly, the vanilla VMamba exhibits stronger rotational robustness on remote sensing datasets than natural image datasets. We attribute both observations to the intrinsic geometric properties of the underlying data distributions. Natural images in these datasets (e.g., ADE20K) typically adhere to canonical upright orientations and lack global rotational symmetry, which limits the benefits of equivariant architectures. In such settings, the parameter reduction induced by group-wise weight sharing may slightly constrain model capacity, leading to marginal performance trade-offs. In contrast, remote sensing images—captured from nadir or aerial perspectives—inherently exhibit stronger rotational symmetry. This enables EQ-VMamba to fully exploit its equivariant inductive bias, yielding markedly improved performance. These findings underscore that the efficacy of equivariant networks is closely coupled with the symmetry properties of the data distribution.

C. Classic Image Super-Resolution

Experimental Settings. We evaluate the classic image super-resolution (SR) performance of EQ-MambaIR on standard benchmarks under the bicubic degradation setting. Following the training protocol of MambaIR [17], all models are trained on DIV2K [83] and Flickr2K [77] datasets, and evaluated on five widely used datasets: Set5 [84], Set14 [85], BSD100 [86], Urban100 [87], and Manga109 [88]. During training, we adopt the L_1 loss function and optimize the network using AdamW [68] with an initial learning rate of 3×10^{-4} and a batch size of 32. The input patch size is set to 64×64. For $\times 2$ SR, models are trained from scratch for 500K iterations. For $\times 3$ and $\times 4$ SR, models are initialized with the pre-trained $\times 2$ weights and subsequently finetuned for 250K iterations.

Experimental Results. Table IV presents the comparison results on standard classic super-resolution benchmarks. The proposed EQ-MambaIR consistently outperforms the MambaIR baseline across all test datasets and all upscaling factors

TABLE V
QUANTITATIVE COMPARISON OF DIFFERENT METHODS ON THE **LIGHTWEIGHT IMAGE SUPER-RESOLUTION** BENCHMARK.

Model	Scale	#Param.	Set5		Set14		BSD100		Urban100		Manga109	
			PSNR	SSIM	PSNR	SSIM	PSNR	SSIM	PSNR	SSIM	PSNR	SSIM
CARN [89]	×2	1,592K	37.76	0.9590	33.52	0.9166	32.09	0.8978	31.92	0.9256	38.36	0.9765
IMDN [90]	×2	694K	38.00	0.9605	33.63	0.9177	32.19	0.8996	32.17	0.9283	38.88	0.9774
LAPAR-A [91]	×2	548K	38.01	0.9605	33.62	0.9183	32.19	0.8999	32.10	0.9283	38.67	0.9772
LatticeNet [92]	×2	756K	38.13	0.9610	33.78	0.9193	32.25	0.9005	32.43	0.9302	-	-
SwinIR-light [53]	×2	910K	38.14	0.9611	33.86	0.9206	32.31	0.9012	32.76	0.9340	39.12	0.9783
ELAN [93]	×2	621K	38.17	0.9611	33.94	0.9207	32.30	0.9012	32.76	0.9340	39.11	0.9782
SRFormer-light [54]	×2	853K	**38.23**	**0.9613**	33.94	0.9209	32.36	0.9019	32.91	0.9353	39.28	**0.9785**
MambaIR-light [17]	×2	859K	38.16	0.9610	**34.00**	**0.9212**	32.34	0.9017	32.92	0.9356	39.31	0.9779
EQ-MambaIR-light	×2	**519K**	38.19	0.9612	33.99	0.9208	**32.37**	**0.9022**	**33.22**	**0.9375**	**39.42**	0.9782
CARN [89]	×3	1,592K	34.29	0.9255	30.29	0.8407	29.06	0.8034	28.06	0.8493	33.50	0.9440
IMDN [90]	×3	703K	34.36	0.9270	30.32	0.8417	29.09	0.8046	28.17	0.8519	33.61	0.9445
LAPAR-A [91]	×3	544K	34.36	0.9267	30.34	0.8421	29.11	0.8054	28.15	0.8523	33.51	0.9441
LatticeNet [92]	×3	765K	34.53	0.9281	30.39	0.8424	29.15	0.8059	28.33	0.8538	-	-
SwinIR-light [53]	×3	886K	34.62	0.9289	30.54	0.8463	29.20	0.8082	28.66	0.8624	33.98	0.9478
ELAN [93]	×3	629K	34.61	0.9288	30.55	0.8463	29.21	0.8081	28.69	0.8624	34.00	0.9478
SRFormer-light [54]	×3	861K	34.67	0.9296	30.57	0.8469	29.26	0.8099	28.81	0.8655	34.19	0.9489
MambaIR-light [17]	×3	867K	34.72	0.9296	30.63	0.8475	29.29	0.8099	29.00	0.8689	34.39	0.9495
EQ-MambaIR-light	×3	**527K**	**34.81**	**0.9302**	**30.66**	**0.8483**	**29.32**	**0.8105**	**29.10**	**0.8708**	**34.48**	**0.9499**
CARN [89]	×4	1,592K	32.13	0.8937	28.60	0.7806	27.58	0.7349	26.07	0.7837	30.47	0.9084
IMDN [90]	×4	715K	32.21	0.8948	28.58	0.7811	27.56	0.7353	26.04	0.7838	30.45	0.9075
LAPAR-A [91]	×4	659K	32.15	0.8944	28.61	0.7818	27.61	0.7366	26.14	0.7871	30.42	0.9074
LatticeNet [92]	×4	777K	32.30	0.8962	28.68	0.7830	27.62	0.7367	26.25	0.7873	-	-
SwinIR-light [53]	×4	897K	32.44	0.8976	28.77	0.7858	27.69	0.7406	26.47	0.7980	30.92	0.9151
ELAN [93]	×4	640K	32.43	0.8975	28.78	0.7858	27.69	0.7406	26.54	0.7982	30.92	0.9150
SRFormer-light [54]	×4	873K	32.51	0.8988	28.82	0.7872	27.73	0.7422	26.67	0.8032	31.17	0.9165
MambaIR-light [17]	×4	879K	32.51	0.8993	28.85	0.7876	27.75	0.7423	26.75	0.8051	31.26	0.9175
EQ-MambaIR-light	×4	**538K**	**32.70**	**0.9006**	**28.89**	**0.7884**	**27.78**	**0.7438**	**26.85**	**0.8082**	**31.31**	**0.9184**

Fig. 10. Visual comparison of image super-resolution results between MambaIR and EQ-MambaIR on Urban100 and Manga109 datasets.

(×2, ×3, and ×4). Notably, these improvements are achieved with approximately half the parameters of the original MambaIR. For example, on the challenging Urban100 dataset, EQ-MambaIR (12M parameters) surpasses MambaIR (20M parameters) by **0.17 dB** and **0.13 dB** in PSNR at ×2 and ×3 scales, respectively. Consistent gains are observed across the remaining test sets, as detailed in the table. Additionally, the qualitative comparisons in Fig. 10 further reveal that EQ-MambaIR substantially improves the reconstruction quality of fine-grained structures and textual elements in degraded images. These results collectively underscore the efficacy of embedding rotation symmetry priors into the Mamba framework for low-level vision tasks.

D. Lightweight Image Super-Resolution

Experimental Settings. We further evaluate EQ-MambaIR under the lightweight SR setting, which imposes more stringent capacity constraints. Following the lightweight protocol established in MambaIR [17], only the DIV2K dataset [83] is used for training. All other experimental configurations, including optimization strategy and evaluation metrics, remain consistent with the classic SR benchmarks.

Experimental Results. Table V presents the comparison results on standard lightweight SR benchmarks. EQ-MambaIR-light outperforms the MambaIR-light baseline on most test datasets and upscaling factors, despite using significantly fewer parameters. For example, on the challenging Urban100 dataset, EQ-MambaIR-light (519K parameters) significantly

TABLE VI
AVERAGE EQUIVARIANCE ERROR OF DIFFERENT MODELS ON p4 ROTATION GROUP (NMSE ↓).

Model	**Image Classification**		**Semantic Segmentation**	
	Untrained	Trained	Untrained	Trained
VMamba-T [14]	0.1721	0.4404	0.3547	0.1958
EQ-VMamba-T	**0.0003**	**0.0003**	**0.0004**	**0.0002**
VMamba-S [14]	0.2017	0.1497	0.3617	0.1809
EQ-VMamba-S	**0.0003**	**0.0003**	**0.0004**	**0.0002**

Model	**Super-Resolution**$\times 2$		**Super-Resolution**$\times 4$	
	Untrained	Trained	Untrained	Trained
MambaIR [17]	0.1548	0.0050	0.0912	0.0099
EQ-MambaIR	**8.6e-5**	**0.0004**	**4.5e-6**	**0.0001**
MambaIR-light [17]	0.4027	0.0061	0.5000	0.0009
EQ-MambaIR-light	**0.0003**	**0.0004**	**3.3e-05**	**6.9e-05**

TABLE VII
ABLATION STUDY ON EQ-CROSS-SCAN AND EQ-VSS BLOCK.

EQ-cross scan	EQ-VSS block	Scale	#Param.	Top-1 (%)	Top-5 (%)
✗	✗	Tiny	30M	87.80	97.70
✓	✗	Tiny	30M	87.88	97.54
✓	✓	Tiny	10M	**88.58**	**98.14**
✗	✗	Small	50M	88.32	97.82
✓	✗	Small	50M	87.76	97.70
✓	✓	Small	17M	**88.70**	**98.22**

TABLE VIII
ABLATION STUDY ON THE GROUP MAMBA BLOCK.

Mamba block type	Scale	#Param.	Top-1 (%)	Top-5 (%)
Independent Mamba block	Tiny	9M	87.98	97.96
Group Mamba block	Tiny	10M	**88.58**	**98.14**
Independent Mamba block	Small	15M	88.04	97.98
Group Mamba block	Small	17M	**88.70**	**98.22**

surpasses MambaIR-light (859K parameters) by **0.30 dB** in PSNR at the $\times 2$ scale, and by **0.10 dB** in PSNR at both $\times 3$ and $\times 4$ scales. On Manga109, EQ-MambaIR-light further achieves gains of **0.11 dB** and **0.09 dB** in PSNR at scales $\times 2$ and $\times 3$, respectively. These results further substantiate the benefits of incorporating rotation equivariance into Mamba-based architectures, particularly in resource-constrained scenarios where parameter efficiency is paramount.

E. Equivariance Verification

To empirically verify the theoretical results of equivariance error presented in Sec. III, we further conduct experiments to quantitatively evaluate the equivariance errors of EQ-VMamba and EQ-MambaIR relative to their non-equivariant counterparts under the $\mathrm{p4}$ rotation group.

Experimental Settings. Following the equivariance evaluation protocol established in [32], we measure equivariance by comparing model predictions on original and transformed inputs. Specifically, for an input image $\boldsymbol{I}$ and a rotation transformation π_G^R sampled from the $\mathrm{p4}$ group, we feed both $\boldsymbol{I}$ and its rotated version $\pi_G^R(\boldsymbol{I})$ into the model $\mathcal{F}(\cdot)$ to obtain their respective outputs. The Normalized Mean Squared Error (NMSE) between $\mathcal{F}\left(\pi_G^R\left(\boldsymbol{I}\right)\right)$ and $\pi_G^R\left(\mathcal{F}\left(\boldsymbol{I}\right)\right)$ serves as the quantitative metric for equivariance error. For high-level and mid-level vision tasks, we compare the equivariance errors of VMamba and EQ-VMamba on the ImageNet-100 and ADE20K test datasets. For low-level vision tasks, we compare the equivariance errors of MambaIR and EQ-MambaIR on the Urban100 dataset for $\times 2$ and $\times 4$ image super-resolution. Since the equivariance of our architecture is an inherent structural property rather than a learned one, we report errors for both randomly initialized (untrained) and fully converged (trained) models to underscore this training-free characteristic.

Experimental Results. Table VI summarizes the average equivariant error under the $\mathrm{p4}$ rotation group. Notably, the equivariance errors of EQ-VMamba and EQ-MambaIR are negligible—effectively approaching zero across all settings—and are several orders of magnitude lower than those of their non-equivariant counterparts. These results empirically validate that EQ-VMamba and EQ-MambaIR achieve robust end-to-end rotation equivariance. Consistent with prior observations in [32], the measured equivariance error of equivariant networks is not exactly zero in practice. This residual error is attributable to floating-point precision limitations in the PyTorch implementation rather than any architectural deficiency. Overall, these empirical findings are in strict alignment with our theoretical derivations.

F. Ablation Study

Effectiveness of Equivariant Modules. To validate the necessity of constructing an end-to-end equivariant architecture, we perform an ablation study on the EQ-cross-scan and EQ-VSS blocks. We progressively replace the vanilla cross-scan and VSS blocks in the baseline with their equivariant counterparts and evaluate the impact on ImageNet-100. As shown in Table VII, employing EQ-cross-scan in isolation yields negligible performance improvements. Significant improvements are realized only when all non-equivariant modules are jointly replaced with their equivariant counterparts, demonstrating that partial equivariance is insufficient and holistic architectural equivariance is essential.

Effectiveness of the Group Mamba block. To assess the importance of feature interaction across the group dimension, we conduct an ablation study on ImageNet-100 in which all group Mamba blocks in EQ-VMamba-T and EQ-VMamba-S are replaced with independent Mamba blocks. The independent variant employs standard shared linear layers instead of EQ-Linear layers to generate the parameters $\boldsymbol{A}$, $\boldsymbol{B}$, and $\boldsymbol{C}$. While still equivariant, this variant lacks inter-group feature interaction. As shown in Table VIII, the group Mamba block significantly outperforms the independent variant, improving Top-1 accuracy by **0.58**% (tiny) and **0.72**% (small), respectively. These results demonstrate that integrating features across the group dimension provides a more effective inductive bias than independent processing of group components.

V. Conclusion

In this paper, we have introduced EQ-VMamba, the first rotation equivariant Mamba-based architecture designed for vision tasks. Motivated by the observed sensitivity of the vanilla VMamba to image rotations, we incorporate rotation equivariance into the Mamba framework through two core innovations: a rotation equivariant cross-scan strategy and the group Mamba blocks. We have provided rigorous theoretical analysis demonstrating that the proposed framework guarantees strict end-to-end 90-degree rotation equivariance. Extensive experiments across multiple benchmarks—including high-level image classification, mid-level semantic segmentation, and low-level image super-resolution—demonstrate that EQ-VMamba consistently outperforms its non-equivariant counterparts, achieving superior accuracy, enhanced rotational robustness, and greater parameter efficiency.

The current EQ-VMamba is designed for the 90-degree rotation group (*i.e.*, the $\mathrm{p4}$ group). A natural extension is to generalize this framework to higher-order rotation groups (e.g., $\mathrm{p8}$) or reflection groups, thereby further broadening the model's equivariant capabilities. Another promising direction involves developing quantitative metrics for characterizing dataset-level symmetries. Our experimental observations in Sec. IV-B indicate that the efficacy of equivariant networks is closely linked to the symmetry properties of the underlying data distribution. Establishing a formal mathematical measure of dataset symmetry could provide principled guidance for predicting the potential benefits of equivariant designs. Furthermore, given that EQ-VMamba employs cyclic parameter sharing within its EQ-Linear layers, exploring hardware-aware acceleration strategies for EQ-Linear operations represents an important direction to fully leverage the linear-complexity efficiency of the Mamba framework.

References

[1] Albert Gu and Tri Dao. Mamba: Linear-time sequence modeling with selective state spaces. In *First conference on language modeling*, 2024.

[2] Karen Simonyan and Andrew Zisserman. Very deep convolutional networks for large-scale image recognition. *arXiv preprint arXiv:1409.1556*, 2014.

[3] Kaiming He, Xiangyu Zhang, Shaoqing Ren, and Sun Jian. Deep residual learning for image recognition. In *Proceedings of the IEEE/CVF conference on computer vision and pattern recognition*, 2016.

[4] Gao Huang, Zhuang Liu, Laurens Van Der Maaten, and Kilian Q Weinberger. Densely connected convolutional networks. In *Proceedings of the IEEE/CVF conference on computer vision and pattern recognition*, pages 4700–4708, 2017.

[5] Mingxing Tan and Quoc Le. Efficientnet: Rethinking model scaling for convolutional neural networks. In *International conference on machine learning*, pages 6105–6114. PMLR, 2019.

[6] Zhuang Liu, Hanzi Mao, Chao-Yuan Wu, Christoph Feichtenhofer, Trevor Darrell, and Saining Xie. A convnet for the 2020s. In *Proceedings of the IEEE/CVF conference on computer vision and pattern recognition*, pages 11976–11986, 2022.

[7] Ashish Vaswani, Noam Shazeer, Niki Parmar, Jakob Uszkoreit, Llion Jones, Aidan N Gomez, Łukasz Kaiser, and Illia Polosukhin. Attention is all you need. *Advances in neural information processing systems*, 30, 2017.

[8] Alexey Dosovitskiy, Lucas Beyer, Alexander Kolesnikov, et al. An image is worth 16x16 words: Transformers for image recognition at scale. In *The Tenth International Conference on Learning Representations*, 2021.

[9] Ze Liu, Yutong Lin, Yue Cao, Han Hu, Yixuan Wei, Zheng Zhang, Stephen Lin, and Baining Guo. Swin transformer: Hierarchical vision transformer using shifted windows. In *Proceedings of the IEEE/CVF international conference on computer vision*, pages 10012–10022, 2021.

[10] Albert Gu, Isys Johnson, Karan Goel, Khaled Saab, Tri Dao, Atri Rudra, and Christopher Ré. Combining recurrent, convolutional, and continuous-time models with linear state space layers. *Advances in neural information processing systems*, 34:572–585, 2021.

[11] Albert Gu, Karan Goel, and Christopher Ré. Efficiently modeling long sequences with structured state spaces. *arXiv preprint arXiv:2111.00396*, 2021.

[12] Jimmy TH Smith, Andrew Warrington, and Scott W Linderman. Simplified state space layers for sequence modeling. *arXiv preprint arXiv:2208.04933*, 2022.

[13] Lianghui Zhu, Bencheng Liao, Qian Zhang, Xinlong Wang, Wenyu Liu, and Xinggang Wang. Vision mamba: Efficient visual representation learning with bidirectional state space model. *arXiv preprint arXiv:2401.09417*, 2024.

[14] Yue Liu, Yunjie Tian, Yuzhong Zhao, Hongtian Yu, Lingxi Xie, Yaowei Wang, Qixiang Ye, Jianbin Jiao, and Yunfan Liu. Vmamba: Visual state space model. In *Advances in Neural Information Processing Systems*, pages 103031–103063, 2024.

[15] Chaodong Xiao, Minghan Li, Zhengqiang Zhang, Deyu Meng, and Lei Zhang. Spatial-mamba: Effective visual state space models via structure-aware state fusion. In *The Fourteenth International Conference on Learning Representations*, 2025.

[16] Zhongchen Zhao, Chaodong Xiao, Hui Lin, Qi Xie, Lei Zhang, and Deyu Meng. Polyline path masked attention for vision transformer. *arXiv preprint arXiv:2506.15940*, 2025.

[17] Hang Guo, Jinmin Li, Tao Dai, Zhihao Ouyang, Xudong Ren, and Shu-Tao Xia. Mambair: A simple baseline for image restoration with state-space model. In *European conference on computer vision*, pages 222–241. Springer, 2024.

[18] Matthew D Zeiler and Rob Fergus. Visualizing and understanding convolutional networks. In *European conference on computer vision*, pages 818–833. Springer, 2014.

[19] Taco Cohen and Max Welling. Group equivariant convolutional networks. In *International conference on machine learning*, pages 2990–2999. PMLR, 2016.

[20] Maurice Weiler and Gabriele Cesa. General e (2)-equivariant steerable cnns. *Advances in neural information processing systems*, 32, 2019.

[21] Zhengyang Shen, Lingshen He, Zhouchen Lin, and Jinwen Ma. Pdo-econvs: Partial differential operator based equivariant convolutions. In *International Conference on Machine Learning*, pages 8697–8706. PMLR, 2020.

[22] Qi Xie, Qian Zhao, Zongben Xu, and Deyu Meng. Fourier series expansion based filter parametrization for equivariant convolutions. *IEEE Transactions on Pattern Analysis and Machine Intelligence*, 45(4):4537–4551, 2022.

[23] Lingshen He, Yuxuan Chen, Yiming Dong, Yisen Wang, Zhouchen Lin, et al. Efficient equivariant network. *Advances in Neural Information Processing Systems*, 34:5290–5302, 2021.

[24] Renjun Xu, Kaifan Yang, Ke Liu, and Fengxiang He. $e(2)$-equivariant vision transformer. In *Uncertainty in Artificial Intelligence*, pages 2356–2366. PMLR, 2023.

[25] Soumyabrata Kundu and Risi Kondor. Steerable transformers for volumetric data. *arXiv preprint arXiv:2405.15932*, 2024.

[26] Taco S Cohen and Max Welling. Steerable cnns. *arXiv preprint arXiv:1612.08498*, 2016.

[27] Daniel E Worrall, Stephan J Garbin, Daniyar Turmukhambetov, and Gabriel J Brostow. Harmonic networks: Deep translation and rotation equivariance. In *Proceedings of the IEEE conference on computer vision and pattern recognition*, pages 5028–5037, 2017.

[28] Yanzhao Zhou, Qixiang Ye, Qiang Qiu, and Jianbin Jiao. Oriented response networks. In *Proceedings of the IEEE Conference on Computer Vision and Pattern Recognition*, pages 519–528, 2017.

[29] Diego Marcos, Michele Volpi, Nikos Komodakis, and Devis Tuia. Rotation equivariant vector field networks. In *Proceedings of the IEEE International Conference on Computer Vision*, pages 5048–5057, 2017.

[30] Maurice Weiler, Fred A Hamprecht, and Martin Storath. Learning steerable filters for rotation equivariant cnns. In *Proceedings of the IEEE Conference on Computer Vision and Pattern Recognition*, pages 849–858, 2018.

[31] David W Romero and Jean-Baptiste Cordonnier. Group equivariant stand-alone self-attention for vision. *arXiv preprint arXiv:2010.00977*, 2020.

[32] Qi Xie, Jiahong Fu, Zongben Xu, and Deyu Meng. Rotation equivariant arbitrary-scale image super-resolution. *IEEE Transactions on Pattern Analysis and Machine Intelligence*, 2025.

[33] Yulu Bai, Jiahong Fu, Qi Xie, and Deyu Meng. A regularization-guided equivariant approach for image restoration. In *Proceedings of the Computer Vision and Pattern Recognition Conference*, pages 2300–2310, 2025.

[34] Sahar Dastani, Ali Bahri, Moslem Yazdanpanah, Mehrdad Noori, David Osowiechi, Gustavo Adolfo Vargas Hakim, Farzad Beizaee, Milad Cheraghalikhani, Arnab Kumar Mondal, Herve Lombaert, et al. Spectral state space model for rotation-invariant visual representation learning. In *Proceedings of the Computer Vision and Pattern Recognition Conference*, pages 23881–23890, 2025.

[35] Michael J Hutchinson, Charline Le Lan, Sheheryar Zaidi, Emilien Dupont, Yee Whye Teh, and Hyunjik Kim. Lietransformer: Equivariant self-attention for lie groups. In *International conference on machine learning*, pages 4533–4543. PMLR, 2021.

[36] Angelos Katharopoulos, Apoorv Vyas, Nikolaos Pappas, and François Fleuret. Transformers are rnns: Fast autoregressive transformers with linear attention. In *International conference on machine learning*, pages 5156–5165. PMLR, 2020.

[37] Rewon Child. Generating long sequences with sparse transformers. *arXiv preprint arXiv:1904.10509*, 2019.

[38] Sepp Hochreiter and Jürgen Schmidhuber. Long short-term memory. *Neural computation*, 9(8):1735–1780, 1997.

[39] Bo Peng, Eric Alcaide, Quentin Anthony, Alon Albalak, Samuel Arcadinho, Stella Biderman, Huanqi Cao, Xin Cheng, Michael Chung, Matteo Grella, et al. Rwkv: Reinventing rnns for the transformer era. *arXiv preprint arXiv:2305.13048*, 2023.

[40] Yutao Sun, Li Dong, Shaohan Huang, Shuming Ma, Yuqing Xia, Jilong Xue, Jianyong Wang, and Furu Wei. Retentive network: A successor to transformer for large language models. *arXiv preprint arXiv:2307.08621*, 2023.

[41] Tao Huang, Xiaohuan Pei, Shan You, Fei Wang, Chen Qian, and Chang Xu. Localmamba: Visual state space model with windowed selective scan. In *European Conference on Computer Vision*, pages 12–22. Springer, 2024.

[42] Yuheng Shi, Minjing Dong, and Chang Xu. Multi-scale vmamba: Hierarchy in hierarchy visual state space model. *Advances in Neural Information Processing Systems*, 37:25687–25708, 2024.

[43] Dongchen Han, Ziyi Wang, Zhuofan Xia, Yizeng Han, Yifan Pu, Chunjiang Ge, Jun Song, Shiji Song, Bo Zheng, and Gao Huang. Demystify mamba in vision: A linear attention perspective. *Advances in neural information processing systems*, 37:127181–127203, 2024.

[44] Hang Guo, Yong Guo, Yaohua Zha, Yulun Zhang, Wenbo Li, Tao Dai, Shu-Tao Xia, and Yawei Li. Mambairv2: Attentive state space restoration. *arXiv preprint arXiv:2411.15269*, 2024.

[45] Zhen Zou, Hu Yu, Jie Huang, and Feng Zhao. Freqmamba: Viewing mamba from a frequency perspective for image deraining. In *Proceedings of the 32nd ACM international conference on multimedia*, pages 1905–1914, 2024.

[46] Yao Teng, Yue Wu, Han Shi, Xuefei Ning, Guohao Dai, Yu Wang, Zhenguo Li, and Xihui Liu. Dim: Diffusion mamba for efficient high-resolution image synthesis. *arXiv preprint arXiv:2405.14224*, 2024.

[47] Kunchang Li, Xinhao Li, Yi Wang, Yinan He, Yali Wang, Limin Wang, and Yu Qiao. Videomamba: State space model for efficient video understanding. In *European conference on computer vision*, pages 237–255. Springer, 2024.

[48] Qinfeng Zhu, Yuanzhi Cai, Yuan Fang, Yihan Yang, Cheng Chen, Lei Fan, and Anh Nguyen. Samba: Semantic segmentation of remotely sensed images with state space model. *Heliyon*, 10(19), 2024.

[49] Sijie Zhao, Hao Chen, Xueliang Zhang, Pengfeng Xiao, Lei Bai, and Wanli Ouyang. Rs-mamba for large remote sensing image dense prediction. *IEEE Transactions on Geoscience and Remote Sensing*, 2024.

[50] Dingkang Liang, Xin Zhou, Wei Xu, Xingkui Zhu, Zhikang Zou, Xiaoqing Ye, Xiao Tan, and Xiang Bai. Pointmamba: A simple state space model for point cloud analysis. *Advances in neural information processing systems*, 37:32653–32677, 2024.

[51] Guowen Zhang, Lue Fan, Chenhang He, Zhen Lei, Zhaoxiang Zhang, and Lei Zhang. Voxel mamba: Group-free state space models for point cloud based 3d object detection. *Advances in Neural Information Processing Systems*, 37:81489–81509, 2024.

[52] Jiacheng Ruan, Jincheng Li, and Suncheng Xiang. Vm-unet: Vision mamba unet for medical image segmentation. *ACM Transactions on Multimedia Computing, Communications and Applications*, 2024.

[53] Jingyun Liang, Jiezhang Cao, Guolei Sun, Kai Zhang, Luc Van Gool, and Radu Timofte. Swinir: Image restoration using swin transformer. In *Proceedings of the IEEE/CVF international conference on computer vision*, pages 1833–1844, 2021.

[54] Yupeng Zhou, Zhen Li, Chun-Le Guo, Song Bai, Ming-Ming Cheng, and Qibin Hou. Srformer: Permuted self-attention for single image super-resolution. In *Proceedings of the IEEE/CVF international conference on computer vision*, pages 12780–12791, 2023.

[55] Dmitry Laptev, Nikolay Savinov, Joachim M Buhmann, and Marc Pollefeys. Ti-pooling: transformation-invariant pooling for feature learning in convolutional neural networks. In *Proceedings of the IEEE conference on computer vision and pattern recognition*, pages 289–297, 2016.

[56] Kihyuk Sohn and Honglak Lee. Learning invariant representations with local transformations. *arXiv preprint arXiv:1206.6418*, 2012.

[57] Alex Krizhevsky, Ilya Sutskever, and Geoffrey E Hinton. Imagenet classification with deep convolutional neural networks. *Advances in neural information processing systems*, 25, 2012.

[58] Emiel Hoogeboom, Jorn WT Peters, Taco S Cohen, and Max Welling. Hexaconv. *arXiv preprint arXiv:1803.02108*, 2018.

[59] Zhengyang Shen, Tiancheng Shen, Zhouchen Lin, and Jinwen Ma. Pdo-es2cnns: Partial differential operator based equivariant spherical cnns. In *Proceedings of the AAAI conference on artificial intelligence*, volume 35, pages 9585–9593, 2021.

[60] Siamak Ravanbakhsh. Universal equivariant multilayer perceptrons. In *International Conference on Machine Learning*, pages 7996–8006. PMLR, 2020.

[61] Tete Xiao, Yingcheng Liu, Bolei Zhou, Yuning Jiang, and Jian Sun. Unified perceptual parsing for scene understanding. In *Proceedings of the European conference on computer vision (ECCV)*, pages 418–434, 2018.

[62] Wenzhe Shi, Jose Caballero, Ferenc Huszár, Johannes Totz, Andrew P Aitken, Rob Bishop, Daniel Rueckert, and Zehan Wang. Real-time single image and video super-resolution using an efficient sub-pixel convolutional neural network. In *Proceedings of the IEEE conference on computer vision and pattern recognition*, pages 1874–1883, 2016.

[63] Jie Hu, Li Shen, and Gang Sun. Squeeze-and-excitation networks. In *Proceedings of the IEEE conference on computer vision and pattern recognition*, pages 7132–7141, 2018.

[64] Hugo Touvron, Matthieu Cord, Matthijs Douze, Francisco Massa, Alexandre Sablayrolles, and Hervé Jégou. Training data-efficient image transformers & distillation through attention. In *International conference on machine learning*, pages 10347–10357. PMLR, 2021.

[65] Alaaeldin Ali, Hugo Touvron, Mathilde Caron, Piotr Bojanowski, Matthijs Douze, Armand Joulin, Ivan Laptev, Natalia Neverova, Gabriel Synnaeve, Jakob Verbeek, et al. Xcit: Cross-covariance image transformers. *Advances in neural information processing systems*, 34:20014–20027, 2021.

[66] ambityga (Kaggle user). Imagenet100 (kaggle dataset). https://www.kaggle.com/datasets/ambityga/imagenet100, 2023. Accessed: 2025-04-21.

[67] Jia Deng, Wei Dong, Richard Socher, et al. Imagenet: A large-scale hierarchical image database. In *Proceedings of the IEEE/CVF conference on computer vision and pattern recognition*, 2009.

[68] Ilya Loshchilov and Frank Hutter. Decoupled weight decay regularization. *arXiv preprint arXiv:1711.05101*, 2017.

[69] Boris T Polyak and Anatoli B Juditsky. Acceleration of stochastic approximation by averaging. *SIAM journal on control and optimization*, 30(4):838–855, 1992.

[70] Bolei Zhou, Hang Zhao, Xavier Puig, et al. Scene parsing through ade20k dataset. In *Proceedings of the IEEE/CVF conference on computer vision and pattern recognition*, 2017.

[71] Mark Everingham, Luc Van Gool, Christopher KI Williams, John Winn, and Andrew Zisserman. The pascal visual object classes (voc) challenge. *International journal of computer vision*, 88(2):303–338, 2010.

[72] Marius Cordts, Mohamed Omran, Sebastian Ramos, Timo Rehfeld, Markus Enzweiler, Rodrigo Benenson, Uwe Franke, Stefan Roth, and Bernt Schiele. The cityscapes dataset for semantic urban scene understanding. In *Proceedings of the IEEE conference on computer vision and pattern recognition*, pages 3213–3223, 2016.

[73] Holger Caesar, Jasper Uijlings, and Vittorio Ferrari. Coco-stuff: Thing and stuff classes in context. In *Proceedings of the IEEE conference on computer vision and pattern recognition*, pages 1209–1218, 2018.

[74] Junjue Wang, Zhuo Zheng, Ailong Ma, Xiaoyan Lu, and Yanfei Zhong. Loveda: A remote sensing land-cover dataset for domain adaptive semantic segmentation. *arXiv preprint arXiv:2110.08733*, 2021.

[75] Franz Rottensteiner, Gunho Sohn, Jaewook Jung, Markus Gerke, Caroline Baillard, Sebastien Benitez, and Uwe Breitkopf. The isprs benchmark on urban object classification and 3d building reconstruction. 2012.

[76] MMSegmentation Contributors. Mmsegmentation, an open source semantic segmentation toolbox, 2020.

[77] Bee Lim, Sanghyun Son, Heewon Kim, Seungjun Nah, and Kyoung Mu Lee. Enhanced deep residual networks for single image super-resolution. In *Proceedings of the IEEE conference on computer vision and pattern recognition workshops*, pages 136–144, 2017.

[78] Yulun Zhang, Kunpeng Li, Kai Li, Lichen Wang, Bineng Zhong, and Yun Fu. Image super-resolution using very deep residual channel attention networks. In *Proceedings of the European conference on computer vision (ECCV)*, pages 286–301, 2018.

[79] Tao Dai, Jianrui Cai, Yongbing Zhang, Shu-Tao Xia, and Lei Zhang. Second-order attention network for single image super-resolution. In *Proceedings of the IEEE/CVF conference on computer vision and pattern recognition*, pages 11065–11074, 2019.

[80] Ben Niu, Weilei Wen, Wenqi Ren, Xiangde Zhang, Lianping Yang, Shuzhen Wang, Kaihao Zhang, Xiaochun Cao, and Haifeng Shen. Single image super-resolution via a holistic attention network. In *European conference on computer vision*, pages 191–207. Springer, 2020.

[81] Hanting Chen, Yunhe Wang, Tianyu Guo, Chang Xu, Yiping Deng, Zhenhua Liu, Siwei Ma, Chunjing Xu, Chao Xu, and Wen Gao. Pre-trained image processing transformer. In *Proceedings of the IEEE/CVF conference on computer vision and pattern recognition*, pages 12299–12310, 2021.

[82] Wenbo Li, Xin Lu, Shengju Qian, Jiangbo Lu, Xiangyu Zhang, and Jiaya Jia. On efficient transformer-based image pre-training for low-level vision. *arXiv preprint arXiv:2112.10175*, 2021.

[83] Radu Timofte, Eirikur Agustsson, Luc Van Gool, Ming-Hsuan Yang, and Lei Zhang. Ntire 2017 challenge on single image super-resolution: Methods and results. In *Proceedings of the IEEE conference on computer vision and pattern recognition workshops*, pages 114–125, 2017.

[84] Marco Bevilacqua, Aline Roumy, Christine Guillemot, and Marie Line Alberi-Morel. Low-complexity single-image super-resolution based on nonnegative neighbor embedding. 2012.

[85] Roman Zeyde, Michael Elad, and Matan Protter. On single image scale-up using sparse-representations. In *Curves and Surfaces: 7th International Conference, Avignon, France, June 24-30, 2010, Revised Selected Papers 7*, pages 711–730. Springer, 2012.

[86] David Martin, Charless Fowlkes, Doron Tal, and Jitendra Malik. A database of human segmented natural images and its application to evaluating segmentation algorithms and measuring ecological statistics. In *Proceedings Eighth IEEE International Conference on Computer Vision. ICCV 2001*, volume 2, pages 416–423. IEEE, 2001.

[87] Jia-Bin Huang, Abhishek Singh, and Narendra Ahuja. Single image super-resolution from transformed self-exemplars. In *Proceedings of the IEEE conference on computer vision and pattern recognition*, pages 5197–5206, 2015.

[88] Yusuke Matsui, Kota Ito, Yuji Aramaki, Azuma Fujimoto, Toru Ogawa, Toshihiko Yamasaki, and Kiyoharu Aizawa. Sketch-based manga retrieval using manga109 dataset. *Multimedia Tools and Applications*, 76:21811–21838, 2017.

[89] Namhyuk Ahn, Byungkon Kang, and Kyung-Ah Sohn. Fast, accurate, and lightweight super-resolution with cascading residual network. In *Proceedings of the European conference on computer vision (ECCV)*, pages 252–268, 2018.

[90] Zheng Hui, Xinbo Gao, Yunchu Yang, and Xiumei Wang. Lightweight image super-resolution with information multi-distillation network. In *Proceedings of the 27th acm international conference on multimedia*, pages 2024–2032, 2019.

[91] Wenbo Li, Kun Zhou, Lu Qi, Nianjuan Jiang, Jiangbo Lu, and Jiaya Jia. Lapar: Linearly-assembled pixel-adaptive regression network for single image super-resolution and beyond. *Advances in Neural Information Processing Systems*, 33:20343–20355, 2020.

[92] Xiaotong Luo, Yuan Xie, Yulun Zhang, Yanyun Qu, Cuihua Li, and Yun Fu. Latticenet: Towards lightweight image super-resolution with lattice block. In *Computer Vision–ECCV 2020: 16th European Conference, Glasgow, UK, August 23–28, 2020, Proceedings, Part XXII 16*, pages 272–289. Springer, 2020.

[93] Xindong Zhang, Hui Zeng, Shi Guo, and Lei Zhang. Efficient long-range attention network for image super-resolution. In *European conference on computer vision*, pages 649–667. Springer, 2022.

"Rotation Equivariant Mamba for Vision Tasks": Supplementary Material

Zhongchen Zhao, Qi Xie, Keyu Huang, Lei Zhang, Deyu Meng, and Zongben Xu

Abstract

This supplementary material provides additional details of the theoretical results and their proofs, as well as further experimental results.

1 Theorems and Proofs

In this section, we introduce the commonly used notations and present detailed proofs of Theorems 1, 2, and 3 stated in the main paper.

1.1 Notations

We employ the following three types of transformations throughout this paper:

(I) $\pi_G^{\mathcal{R}}(\cdot)$: rotation in the spatial domain without altering the group dimension. As shown in Fig. 1(a), this transformation is typically applied to input images.

(II) $\pi_G^{\mathcal{RS}}(\cdot)$: rotation in the spatial domain combined with cyclic shifting along the group dimension, as shown in Fig. 1(b). Formally, for any feature map $\boldsymbol{X} \in \mathbb{R}^{H\times W\times C\times T}$, we have:

$$\left(\pi_{\hat{G}}^{\mathcal{RS}}(\boldsymbol{X})\right)^G = \pi_{\hat{G}}^{\mathcal{R}}\left(\boldsymbol{X}^{\hat{G}^{-1}G}\right), \quad \forall G, \hat{G} \in \mathcal{G}. \tag{1}$$

This transformation is particularly common in prior equivariant CNNs and is typically applied to feature maps that carry a group dimension.

(III) $\pi_G^{\mathcal{S}}(\cdot)$: cyclic shifting along the group dimension, with no change in the spatial domain. As shown in Fig. 1(c), for a feature map $\boldsymbol{X}$, we have

$$\left(\pi_{\hat{G}}^{\mathcal{S}}(\boldsymbol{X})\right)^G = \boldsymbol{X}^{\hat{G}^{-1}G}, \quad \forall G, \hat{G} \in \mathcal{G}. \tag{2}$$

This transformation is applied to the scanning order of Mamba in our proposed framework.

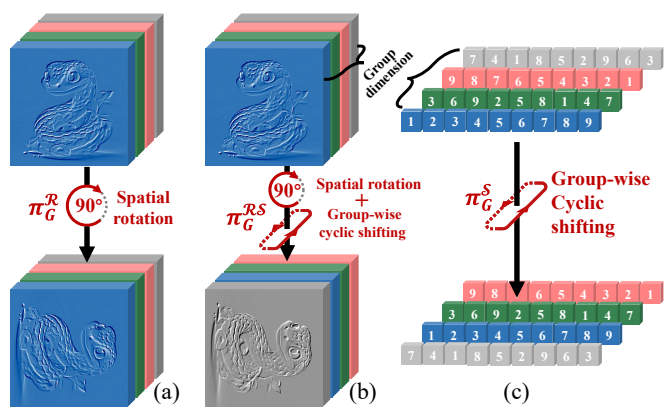

Fig. 1. Illustration of the group dimension (indexed by colors) and three fundamental transformation operators utilized in our equivariant framework. (a)-(c) illustrate $\pi_G^{\mathcal{R}}(\cdot)$, $\pi_G^{\mathcal{RS}}(\cdot)$, and $\pi_G^{\mathcal{S}}(\cdot)$, respectively.

1.2 Proof of Theorem 1

In the main text, the EQ-cross-scan operator $\tau_{eq}(\cdot)$ is defined as

$$\boldsymbol{x} = \tau_{eq}\left(\boldsymbol{X}\right), \text{ with } \boldsymbol{x}^G = \tau\left(\pi_{G^{-1}}^{\mathcal{R}}\left(\boldsymbol{X}^G\right)\right), \; G \in \mathcal{G}, \tag{3}$$

where $\boldsymbol{X} \in \mathbb{R}^{H\times W\times C\times 4}$ denotes the group-structured 2D feature map, $\boldsymbol{x} \in \mathbb{R}^{HW\times C\times 4}$ denotes the resulting 1D feature sequences, and $\tau\left(\cdot\right)$ represents the base scanning path (*i.e.*, the standard matrix-to-vector unfolding).

Symmetrically, the inverse operation of EQ-cross-scan, termed EQ-cross-merge $\tau_{eq}^{inv}(\cdot)$, is defined as

$$\hat{X} = \tau_{eq}^{inv}\left(\boldsymbol{x}\right), \text{ with } \hat{X}^G = \pi_G^{\mathcal{R}}\left(\tau^{inv}\left(\boldsymbol{x}^G\right)\right), \; G \in \mathcal{G}, \tag{4}$$

where $\tau^{inv}\left(\cdot\right)$ denotes the standard vector-to-matrix folding.

Based on these definitions, we establish the following theorem.

Zhongchen Zhao, Qi Xie, Keyu Huang, Deyu Meng, and Zongben Xu are with the School of Mathematics and Statistics, Xi'an Jiaotong University, Shaanxi, P.R. China (e-mail: zhongchenzhao@stu.xjtu.edu.cn, xie.qi@mail.xjtu.edu.cn, keyuhuang@stu.xjtu.edu.cn, dymeng@mail.xjtu.edu.cn, zbxu@mail.xjtu.edu.cn). Lei Zhang is with the Department of Computing, the Hong Kong Polytechnic University, Hong Kong, P.R. China (e-mail: cslzhang@comp.polyu.edu.hk).

Theorem 1. *Let $\boldsymbol{X} \in \mathbb{R}^{H\times W\times C\times 4}$ be a group-structured feature map and let $\boldsymbol{x} \in \mathbb{R}^{HW\times C\times 4}$ be a group-structured feature sequence. Let $\tau_{eq}(\cdot)$ and $\tau_{eq}^{inv}(\cdot)$ denote the EQ-cross-scan and EQ-cross-merge operators defined in* (3) *and* (4)*, respectively. For any group element $\hat{G} \in \mathcal{G}$, the following equivariance properties hold:*

$$\tau_{eq}\left(\pi_{\hat{G}}^{\mathcal{RS}}\left(\boldsymbol{X}\right)\right) = \pi_{\hat{G}}^{\mathcal{S}}\left(\tau_{eq}\left(\boldsymbol{X}\right)\right), \tag{5}$$

$$\tau_{eq}^{inv}\left(\pi_{\hat{G}}^{\mathcal{S}}\left(\boldsymbol{x}\right)\right) = \pi_{\hat{G}}^{\mathcal{RS}}\left(\tau_{eq}^{inv}\left(\boldsymbol{x}\right)\right). \tag{6}$$

Proof. **1) Equivariance of EQ-cross-scan.** According to the definition of $\tau_{eq}(\cdot)$ in (3), for any $\hat{G} \in \mathcal{G}$, the G-th component of the left-hand side of Eq. (5) is

$$\left(\tau_{eq}\left(\pi_{\hat{G}}^{\mathcal{RS}}\left(\boldsymbol{X}\right)\right)\right)^{G} = \tau\left(\pi_{G^{-1}}^{\mathcal{R}}\left(\left(\pi_{\hat{G}}^{\mathcal{RS}}\left(\boldsymbol{X}\right)\right)^{G}\right)\right). \tag{7}$$

Meanwhile, according to the definition of $\pi_{\hat{G}}^{\mathcal{S}}\left(\cdot\right)$ in Eq. (2), we have

$$\boldsymbol{x}^{\hat{G}^{-1}G} = (\pi_{\hat{G}}^{\mathcal{S}}(\boldsymbol{x}))^{G}. \tag{8}$$

Expanding Eq. (7) step by step, we obtain

$$\begin{aligned}
\left(\tau_{eq}\left(\pi_{\hat{G}}^{\mathcal{RS}}\left(\boldsymbol{X}\right)\right)\right)^{G} &= \tau\left(\pi_{G^{-1}}^{\mathcal{R}}\left(\left(\pi_{\hat{G}}^{\mathcal{RS}}\left(\boldsymbol{X}\right)\right)^{G}\right)\right) && \text{(by Eq. (7))}\\
&= \tau\left(\pi_{G^{-1}}^{\mathcal{R}}\left(\pi_{\hat{G}}^{\mathcal{R}}\left(\boldsymbol{X}^{\hat{G}^{-1}G}\right)\right)\right) && \text{(by Eq. (1))}\\
&= \tau\left(\pi_{G^{-1}\hat{G}}^{\mathcal{R}}\left(\boldsymbol{X}^{\hat{G}^{-1}G}\right)\right) && (\pi_{G^{-1}}^{\mathcal{R}} \circ \pi_{\hat{G}}^{\mathcal{R}} = \pi_{G^{-1}\hat{G}}^{\mathcal{R}})\\
&= \left(\tau_{eq}\left(\boldsymbol{X}\right)\right)^{\hat{G}^{-1}G} && \text{(by Eq. (3))}\\
&= \left(\pi_{\hat{G}}^{\mathcal{S}}\left(\tau_{eq}\left(\boldsymbol{X}\right)\right)\right)^{G}. && \text{(by Eq. (8))}
\end{aligned} \tag{9}$$

Since the above holds for all $G \in \mathcal{G}$, the equivariance of EQ-cross-scan (Eq. (5)) is established.

2) Equivariance of EQ-cross-merge. According to the definition of $\tau_{eq}^{inv}(\cdot)$ in (4), for any $\hat{G} \in \mathcal{G}$, the G-th component of the left-hand side of Eq. (6) is

$$\left(\tau_{eq}^{inv}\left(\pi_{\hat{G}}^{\mathcal{S}}\left(\boldsymbol{x}\right)\right)\right)^{G} = \pi_{G}^{\mathcal{R}}\left(\tau^{inv}\left(\left(\pi_{\hat{G}}^{\mathcal{S}}\left(\boldsymbol{x}\right)\right)^{G}\right)\right). \tag{10}$$

Meanwhile, according to the definition of $\pi_{\hat{G}}^{\mathcal{RS}}\left(\cdot\right)$ in Eq. (1), we have

$$\pi_{\hat{G}}^{\mathcal{R}}\left(\boldsymbol{X}^{\hat{G}^{-1}G}\right) = \left(\pi_{\hat{G}}^{\mathcal{RS}}\left(\boldsymbol{X}\right)\right)^{G}. \tag{11}$$

Expanding Eq. (10) step by step, we obtain

$$\begin{aligned}
\left(\tau_{eq}^{inv}\left(\pi_{\hat{G}}^{\mathcal{S}}\left(\boldsymbol{x}\right)\right)\right)^{G} &= \pi_{G}^{\mathcal{R}}\left(\tau^{inv}\left(\left(\pi_{\hat{G}}^{\mathcal{S}}\left(\boldsymbol{x}\right)\right)^{G}\right)\right) && \text{(by Eq. (10))}\\
&= \pi_{G}^{\mathcal{R}}\left(\tau^{inv}\left(\boldsymbol{x}^{\hat{G}^{-1}G}\right)\right) && \text{(by Eq. (2))}\\
&= \pi_{\hat{G}}^{\mathcal{R}}\left(\pi_{\hat{G}^{-1}G}^{\mathcal{R}}\left(\tau^{inv}\left(\boldsymbol{x}^{\hat{G}^{-1}G}\right)\right)\right) && (\pi_{G}^{\mathcal{R}} = \pi_{\hat{G}}^{\mathcal{R}} \circ \pi_{\hat{G}^{-1}G}^{\mathcal{R}})\\
&= \pi_{\hat{G}}^{\mathcal{R}}\left(\left(\tau_{eq}^{inv}\left(\boldsymbol{x}\right)\right)^{\hat{G}^{-1}G}\right) && \text{(by Eq. (4))}\\
&= \left(\pi_{\hat{G}}^{\mathcal{RS}}\left(\tau_{eq}^{inv}\left(\boldsymbol{x}\right)\right)\right)^{G}. && \text{(by Eq. (11))}
\end{aligned} \tag{12}$$

Since the above holds for all $G \in \mathcal{G}$, the equivariance of EQ-cross-merge (Eq. (6)) is established.

Combining the above two parts, Theorem 1 is proved. □

1.3 Proof of Theorem 2

In the main text, the group Mamba block $\mathrm{SSM}_{\mathrm{eq}}(\cdot)$ is defined as

$$\boldsymbol{y} = \mathrm{SSM}_{\mathrm{eq}}\left(\boldsymbol{x}; \boldsymbol{A}, \boldsymbol{B}, \boldsymbol{C}, D\right), \text{ with } \boldsymbol{y}^{G} = \mathrm{SSM}\left(\boldsymbol{x}^{G}; \boldsymbol{A}^{G}, \boldsymbol{B}^{G}, \boldsymbol{C}^{G}, D\right), \ \forall G \in \mathcal{G}, \tag{13}$$

where $\boldsymbol{x}, \boldsymbol{y} \in \mathbb{R}^{HW\times C\times 4}$ denote the input and output sequences, respectively, and $D \in \mathbb{R}$ is a shared scalar parameter. The input-dependent parameters $\boldsymbol{A} \in \mathbb{R}^{HW\times N\times N\times C\times 4}$ and $\boldsymbol{B}, \boldsymbol{C} \in \mathbb{R}^{HW\times N\times 4}$ are generated via EQ-Linear layers [1], [2] as follows:

$$\boldsymbol{A} = \tau_{eq}\left(\delta_a\left(\Upsilon_a\left(\boldsymbol{X}\right)\right)\right), \ \boldsymbol{B} = \tau_{eq}\left(\delta_b\left(\Upsilon_b\left(\boldsymbol{X}\right)\right)\right), \ \boldsymbol{C} = \tau_{eq}\left(\delta_c\left(\Upsilon_c\left(\boldsymbol{X}\right)\right)\right), \tag{14}$$

where $\delta_a\left(\cdot\right)$, $\delta_b\left(\cdot\right)$, and $\delta_c\left(\cdot\right)$ denote the element-wise non-linear operations and reshape operations that satisfy rotation equivariance, and $\mathrm{SSM}\left(\cdot\right)$ denotes the standard Mamba formulation applied to each group component of the input feature sequences. Concretely, for $k = 1, 2, \cdots, C$ and $\forall G \in \mathcal{G}$,

$$\begin{aligned}
\boldsymbol{h}_{i,k}^{G} &= \boldsymbol{A}_{i,k}^{G}\boldsymbol{h}_{i-1,k}^{G} + \boldsymbol{B}_{i,k}^{G}\boldsymbol{x}_{i,k}^{G},\\
\boldsymbol{y}_{i,k}^{G} &= \boldsymbol{C}_{i,k}^{G\top}\boldsymbol{h}_{i,k}^{G} + D\boldsymbol{x}_{i,k}^{G}.
\end{aligned} \tag{15}$$

Based on this formulation, we establish the following theorem.

Theorem 2. *Let $\boldsymbol{X} \in \mathbb{R}^{H\times W\times C\times 4}$ be a group-structured feature map. Given the group Mamba block $\mathrm{SSM}_{\mathrm{eq}}(\cdot)$ defined in* (13) *with parameters $\boldsymbol{A}$, $\boldsymbol{B}$, and $\boldsymbol{C}$ derived according to* (14)*, the following equivariance property holds for any $\hat{G} \in \mathcal{G}$:*

$$\mathrm{SSM}_{\mathrm{eq}}\left(\pi_{\hat{G}}^{\mathcal{S}}\left(\boldsymbol{x}\right); \pi_{\hat{G}}^{\mathcal{S}}\left(\boldsymbol{A}\right), \pi_{\hat{G}}^{\mathcal{S}}\left(\boldsymbol{B}\right), \pi_{\hat{G}}^{\mathcal{S}}\left(\boldsymbol{C}\right), D\right) = \pi_{\hat{G}}^{\mathcal{S}}\left(\mathrm{SSM}_{\mathrm{eq}}\left(\boldsymbol{x}; \boldsymbol{A}, \boldsymbol{B}, \boldsymbol{C}, D\right)\right). \tag{16}$$

Proof. **1) Equivariance of Parameters $\boldsymbol{A}$, $\boldsymbol{B}$, and $\boldsymbol{C}$.** According to the equivariance property of EQ-Linear layers, the following equation holds for any $\hat{G} \in \mathcal{G}$:

$$\Upsilon_a\left(\pi_{\hat{G}}^{\mathcal{RS}}\left(\boldsymbol{X}\right)\right) = \pi_{\hat{G}}^{\mathcal{RS}}\left(\Upsilon_a\left(\boldsymbol{X}\right)\right) \tag{17}$$

According to Theorem 1, we have

$$\begin{aligned}
\tau_{eq}\left(\delta_a\left(\Upsilon_a\left(\pi_{\hat{G}}^{\mathcal{RS}}\left(\boldsymbol{X}\right)\right)\right)\right) &= \tau_{eq}\left(\delta_a\left(\pi_{\hat{G}}^{\mathcal{RS}}\left(\Upsilon_a\left(\boldsymbol{X}\right)\right)\right)\right) && \text{(by Eq. (17))}\\
&= \tau_{eq}\left(\pi_{\hat{G}}^{\mathcal{RS}}\left(\delta_a\left(\Upsilon_a\left(\boldsymbol{X}\right)\right)\right)\right) && (\ \delta_a \circ \pi_{\hat{G}}^{\mathcal{RS}} = \pi_{\hat{G}}^{\mathcal{RS}} \circ \delta_a\ )\\
&= \pi_{\hat{G}}^{\mathcal{S}}\left(\tau_{eq}\left(\delta_a\left(\Upsilon_a\left(\boldsymbol{X}\right)\right)\right)\right) && \text{(by Eq. (5) in Theorem 1)}\\
&= \pi_{\hat{G}}^{\mathcal{S}}\left(\boldsymbol{A}\right). && \text{(by Eq. (14))}
\end{aligned} \tag{18}$$

Eq. (18) shows that a spatial rotation combined with a group-wise cyclic shifting applied to the feature map $\boldsymbol{X}$ induces a corresponding group-wise cyclic shifting on the output parameters $\boldsymbol{A}$. By analogous reasoning, the same equivariance property holds for the operators generating parameters $\boldsymbol{B}$ and $\boldsymbol{C}$:

$$\tau_{eq}\left(\delta_b\left(\Upsilon_b\left(\pi_{\hat{G}}^{\mathcal{RS}}\left(\boldsymbol{X}\right)\right)\right)\right) = \pi_{\hat{G}}^{\mathcal{S}}\left(\boldsymbol{B}\right), \quad \tau_{eq}\left(\delta_c\left(\Upsilon_c\left(\pi_{\hat{G}}^{\mathcal{RS}}\left(\boldsymbol{X}\right)\right)\right)\right) = \pi_{\hat{G}}^{\mathcal{S}}\left(\boldsymbol{C}\right). \tag{19}$$

2) Equivariance of Group Mamba Blocks. According to the definition of $\mathrm{SSM}_{\mathrm{eq}}(\cdot)$ in Eq. (13), for any $\hat{G} \in \mathcal{G}$, the G-th component of the left-hand side of Eq. (16) is

$$\begin{aligned}
\left(\mathrm{SSM}_{\mathrm{eq}}\left(\pi_{\hat{G}}^{\mathcal{S}}\left(\boldsymbol{x}\right); \pi_{\hat{G}}^{\mathcal{S}}\left(\boldsymbol{A}\right), \pi_{\hat{G}}^{\mathcal{S}}\left(\boldsymbol{B}\right), \pi_{\hat{G}}^{\mathcal{S}}\left(\boldsymbol{C}\right), D\right)\right)^G &= \mathrm{SSM}\left(\left(\pi_{\hat{G}}^{\mathcal{S}}\left(\boldsymbol{x}\right)\right)^G; \left(\pi_{\hat{G}}^{\mathcal{S}}\left(\boldsymbol{A}\right)\right)^G, \left(\pi_{\hat{G}}^{\mathcal{S}}\left(\boldsymbol{B}\right)\right)^G, \left(\pi_{\hat{G}}^{\mathcal{S}}\left(\boldsymbol{C}\right)\right)^G, D\right) && \text{(by Eq. (13))}\\
&= \mathrm{SSM}\left(\boldsymbol{x}^{\hat{G}^{-1}G}; \boldsymbol{A}^{\hat{G}^{-1}G}, \boldsymbol{B}^{\hat{G}^{-1}G}, \boldsymbol{C}^{\hat{G}^{-1}G}, D\right) && \text{(by Eq. (2))}\\
&= \left(\mathrm{SSM}_{\mathrm{eq}}\left(\boldsymbol{x}; \boldsymbol{A}, \boldsymbol{B}, \boldsymbol{C}, D\right)\right)^{\hat{G}^{-1}G} && \text{(by Eq. (13))}\\
&= \left(\pi_{\hat{G}}^{\mathcal{S}}\left(\mathrm{SSM}_{\mathrm{eq}}\left(\boldsymbol{x}; \boldsymbol{A}, \boldsymbol{B}, \boldsymbol{C}, D\right)\right)\right)^G. && \text{(by Eq. (2))}
\end{aligned} \tag{20}$$

Thus, Theorem 2 is proved. □

1.4 Proof of Theorem 3

By combining EQ-cross-scan (Eq. (3)), group Mamba blocks (Eq. (13)), and EQ-cross-merge (Eq. (4)), we formulate the equivariant EQ-VSS block for an input feature map $\boldsymbol{X} \in \mathbb{R}^{H\times W\times C\times T}$ as

$$\mathrm{VSS}_{\mathrm{eq}}(\boldsymbol{X}) = \tau_{eq}^{inv}\left(\mathrm{SSM}_{\mathrm{eq}}\left(\tau_{eq}\left(\boldsymbol{X}\right); \boldsymbol{A}, \boldsymbol{B}, \boldsymbol{C}, D\right)\right). \tag{21}$$

Building on Theorems 1 and 2, we establish the rotation equivariance of the entire EQ-VSS block.

Theorem 3. *Under the same conditions as Theorems 1 and 2, the EQ-VSS block defined in Eq.* (21) *satisfies the equivariance property for any $\hat{G} \in \mathcal{G}$:*

$$\mathrm{VSS}_{\mathrm{eq}}\left(\pi_{\hat{G}}^{\mathcal{RS}}\left(\boldsymbol{X}\right)\right) = \pi_{\hat{G}}^{\mathcal{RS}}\left(\mathrm{VSS}_{\mathrm{eq}}\left(\boldsymbol{X}\right)\right). \tag{22}$$

Proof. Note that the input-dependent parameters $\boldsymbol{A}$, $\boldsymbol{B}$, and $\boldsymbol{C}$ in the group Mamba block $\mathrm{SSM}_{\mathrm{eq}}(\cdot)$ are derived from the feature map $\boldsymbol{X}$ via EQ-Linear layers, as specified in Eq. (14). Therefore, as established in Eqs. (18) and (19), when $\boldsymbol{X}$ undergoes a spatial rotation together with a group-wise cyclic shifting, the resulting parameters $\boldsymbol{A}$, $\boldsymbol{B}$, and $\boldsymbol{C}$ correspondingly undergo a group-wise cyclic shifting. Specifically, for any $\hat{G} \in \mathcal{G}$:

$$\tau_{eq}\left(\delta_a\left(\Upsilon_a\left(\pi_{\hat{G}}^{\mathcal{RS}}\left(\boldsymbol{X}\right)\right)\right)\right) = \pi_{\hat{G}}^{\mathcal{S}}\left(\boldsymbol{A}\right), \quad \tau_{eq}\left(\delta_b\left(\Upsilon_b\left(\pi_{\hat{G}}^{\mathcal{RS}}\left(\boldsymbol{X}\right)\right)\right)\right) = \pi_{\hat{G}}^{\mathcal{S}}\left(\boldsymbol{B}\right), \quad \tau_{eq}\left(\delta_c\left(\Upsilon_c\left(\pi_{\hat{G}}^{\mathcal{RS}}\left(\boldsymbol{X}\right)\right)\right)\right) = \pi_{\hat{G}}^{\mathcal{S}}\left(\boldsymbol{C}\right). \tag{23}$$

According to the definition of EQ-VSS block $\mathrm{VSS}_{\mathrm{eq}}(\cdot)$ in Eq. (21), we expand the left-hand side of Eq. (22) and apply the established equivariance results sequentially:

$$\begin{aligned}
\mathrm{VSS}_{\mathrm{eq}}\left(\pi_{\hat{G}}^{\mathcal{RS}}\left(\boldsymbol{X}\right)\right) &= \tau_{eq}^{inv}\left(\mathrm{SSM}_{\mathrm{eq}}\left(\tau_{eq}\left(\pi_{\hat{G}}^{\mathcal{RS}}\left(\boldsymbol{X}\right)\right); \pi_{\hat{G}}^{\mathcal{S}}\left(\boldsymbol{A}\right), \pi_{\hat{G}}^{\mathcal{S}}\left(\boldsymbol{B}\right), \pi_{\hat{G}}^{\mathcal{S}}\left(\boldsymbol{C}\right), D\right)\right) && \text{(by Eq. (21) and Eq. (23))}\\
&= \tau_{eq}^{inv}\left(\mathrm{SSM}_{\mathrm{eq}}\left(\pi_{\hat{G}}^{\mathcal{S}}\left(\tau_{eq}\left(\boldsymbol{X}\right)\right); \pi_{\hat{G}}^{\mathcal{S}}\left(\boldsymbol{A}\right), \pi_{\hat{G}}^{\mathcal{S}}\left(\boldsymbol{B}\right), \pi_{\hat{G}}^{\mathcal{S}}\left(\boldsymbol{C}\right), D\right)\right) && \text{(by Eq. (5) in Theorem 1)}\\
&= \tau_{eq}^{inv}\left(\pi_{\hat{G}}^{\mathcal{S}}\left(\mathrm{SSM}_{\mathrm{eq}}\left(\tau_{eq}\left(\boldsymbol{X}\right); \boldsymbol{A}, \boldsymbol{B}, \boldsymbol{C}, D\right)\right)\right) && \text{(by Eq. (16) in Theorem 2)}\\
&= \pi_{\hat{G}}^{\mathcal{RS}}\left(\tau_{eq}^{inv}\left(\mathrm{SSM}_{\mathrm{eq}}\left(\tau_{eq}\left(\boldsymbol{X}\right); \boldsymbol{A}, \boldsymbol{B}, \boldsymbol{C}, D\right)\right)\right) && \text{(by Eq. (6) in Theorem 1)}\\
&= \pi_{\hat{G}}^{\mathcal{RS}}\left(\mathrm{VSS}_{\mathrm{eq}}\left(\boldsymbol{X}\right)\right). && \text{(by Eq. (21))}
\end{aligned} \tag{24}$$

Thus, Theorem 3 is proved. □

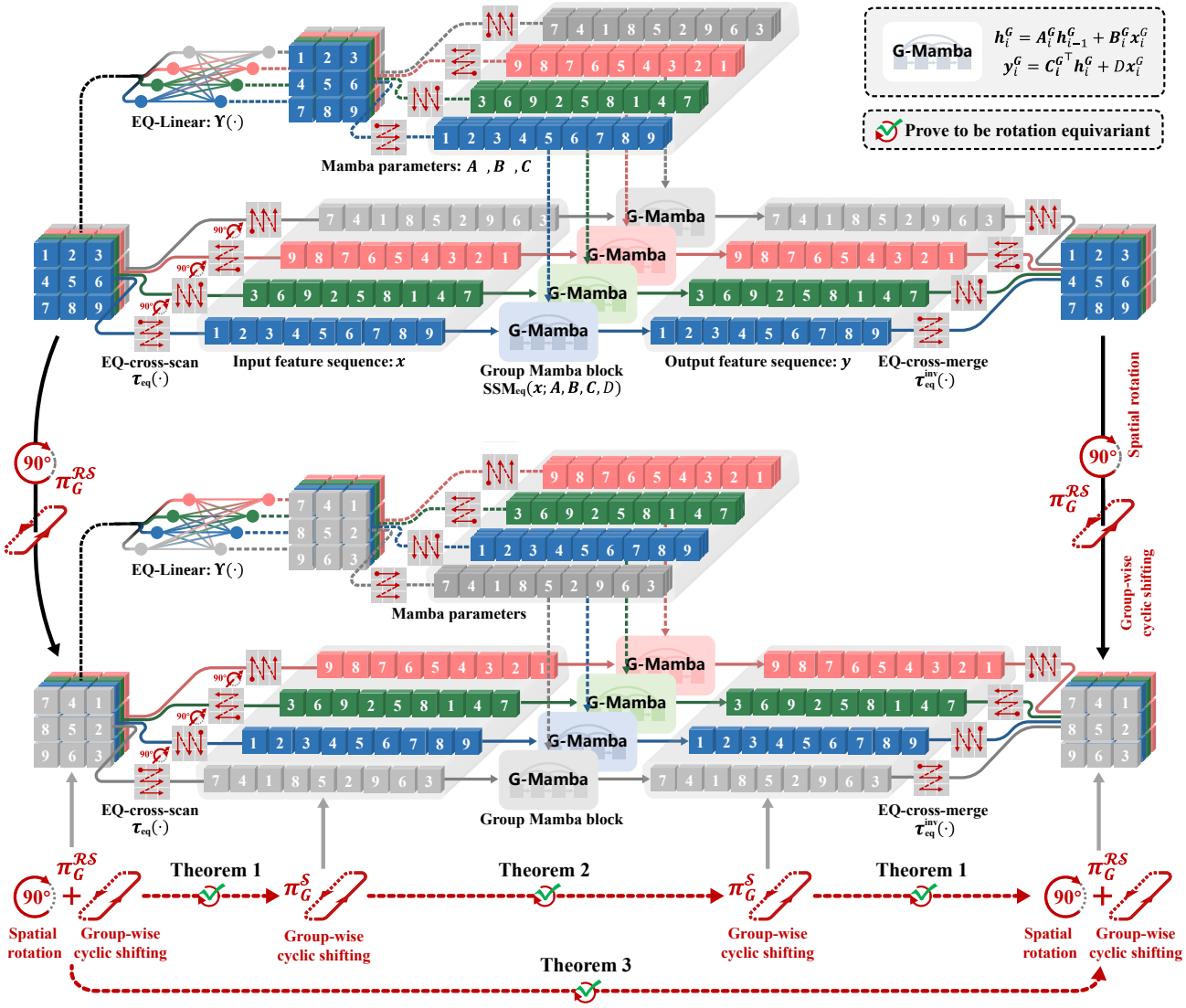

Fig. 2. **Upper**: Detailed illustration of the rotation equivariance of the proposed EQ-VSS block. When the input image is rotated clockwise by 90°, the corresponding feature map undergoes a coupled transformation composed of a spatial rotation and a group-wise cyclic shifting. The transformed feature map preserves strict equivariance throughout the EQ-cross-scan, group Mamba blocks, and EQ-cross-merge, yielding a fully equivariant output. **Bottom**: Illustration of the theoretical results, showing the correspondence between each theorem and its respective network module.

Fig. 2 provides an intuitive illustration of the EQ-VSS block $\mathrm{VSS}_{\mathrm{eq}}(\cdot)$, depicting the detailed computation process, the resulting output when the input feature map undergoes a spatial rotation combined with a group-wise cyclic shifting, and the corresponding theorems that guarantee equivariance at each stage.

2 More Experimental Results

2.1 Comparison with Other Equivariant Networks

To further validate the superiority of the proposed Mamba-based equivariant network, we compare EQ-MambaIR with state-of-the-art CNN-based equivariant networks [3]–[6] and the ViT-based equivariant network [2] on $\times 2$ image super-resolution tasks under the $\mathrm{p4}$ rotation group.

Experimental Settings. Following the training protocol of F-Conv [6], we use 800 images from the DIV2K dataset [7] for training and evaluate on four standard benchmarks: Urban100 [8], BSD100 [9], Set14 [10], and Set5 [11]. The input patch size is set to 96×96, and all models are trained from scratch for 150K iterations. The comparison methods include CNN-based equivariant networks—G-CNN [3], E2-CNN [4], PDO-eConv [5], and F-Conv [6]—as well as the ViT-based equivariant network EQ-SwinIR [2]. All CNN-based equivariant networks are implemented based on the RCAN [12] backbone. For a fair comparison, we reduce the number of feature channels in EQ-MambaIR from 180 to 64 (denoted as EQ-MambaIR*) to maintain a model size comparable to those of the other equivariant networks. All equivariant networks are reproduced under the same experimental settings.

Experimental Results. Table 1 presents the comparison results of different equivariant networks on $\times 2$ image super-resolution benchmarks. Under a comparable model size, EQ-MambaIR* achieves the best performance on all four bench-

TABLE 1
Quantitative comparison of different **equivariant networks** under the $p4$ rotation group on the **image super-resolution** ($\times 2$ scale) benchmark.

Model	Architecture	#Param.	Urban100 [8]		BSD100 [9]		Set14 [10]		Set5 [11]	
			PSNR	SSIM	PSNR	SSIM	PSNR	SSIM	PSNR	SSIM
G-CNN [3]	CNN	8.6M	32.40	0.9324	32.24	0.9036	33.73	0.9210	38.05	0.9623
E2-CNN [4]	CNN	3.9M	31.38	0.9224	32.00	0.9006	33.32	0.9172	37.73	0.9610
PDO-eConv [5]	CNN	3.2M	30.70	0.9132	31.81	0.8978	33.09	0.9153	37.54	0.9602
F-Conv [6]	CNN	8.7M	32.81	0.9351	32.31	0.9043	33.83	0.9217	38.20	0.9627
EQ-SwinIR [2]	Transformer	5.3M	32.84	0.9358	**32.37**	0.9046	33.91	0.9229	38.21	0.9628
EQ-MambaIR*	SSM	6.1M	**33.06**	**0.9374**	**32.37**	**0.9051**	**34.05**	**0.9235**	**38.27**	**0.9630**

EQ-MambaIR* denotes the parameter-reduced variant of EQ-MambaIR for a fair comparison with other equivariant networks.

marks, surpassing the strongest CNN-based competitor F-Conv by **0.25 dB** and **0.22 dB** in PSNR on Urban100 and Set14, respectively. Compared with the Transformer-based equivariant network EQ-SwinIR, EQ-MambaIR* also achieves consistent improvements across all datasets, with PSNR gains of **0.22 dB** on Urban100, demonstrating the superior capability of the SSM-based architecture in capturing long-range dependencies for equivariant image restoration. These results highlight that incorporating rotation equivariance into the Mamba framework yields a more effective and parameter-efficient solution compared to both CNN-based and Transformer-based equivariant counterparts.

2.2 More Visualization Results

Semantic Segmentation. Fig. 3 presents additional qualitative comparisons of segmentation results between VMamba and EQ-VMamba on the LoveDA, PASCAL VOC 2012, and Cityscapes datasets. Compared with VMamba, EQ-VMamba produces more accurate segmentation predictions, especially around object boundaries and small structures, while exhibiting stronger robustness under rotational variations. These qualitative results are consistent with the quantitative improvements reported in the main paper and further demonstrate the advantage of incorporating rotation equivariance into the visual Mamba framework.

Image Super-Resolution. Fig. 4 provides additional qualitative comparisons between MambaIR and EQ-MambaIR on the Urban100 and Manga109 datasets. As shown in the figure, EQ-MambaIR reconstructs noticeably sharper edges, clearer textures, and more faithful structural details than MambaIR, particularly in regions containing repeated patterns and fine-grained geometric structures. These observations further verify the effectiveness of the proposed equivariant design for image super-resolution.

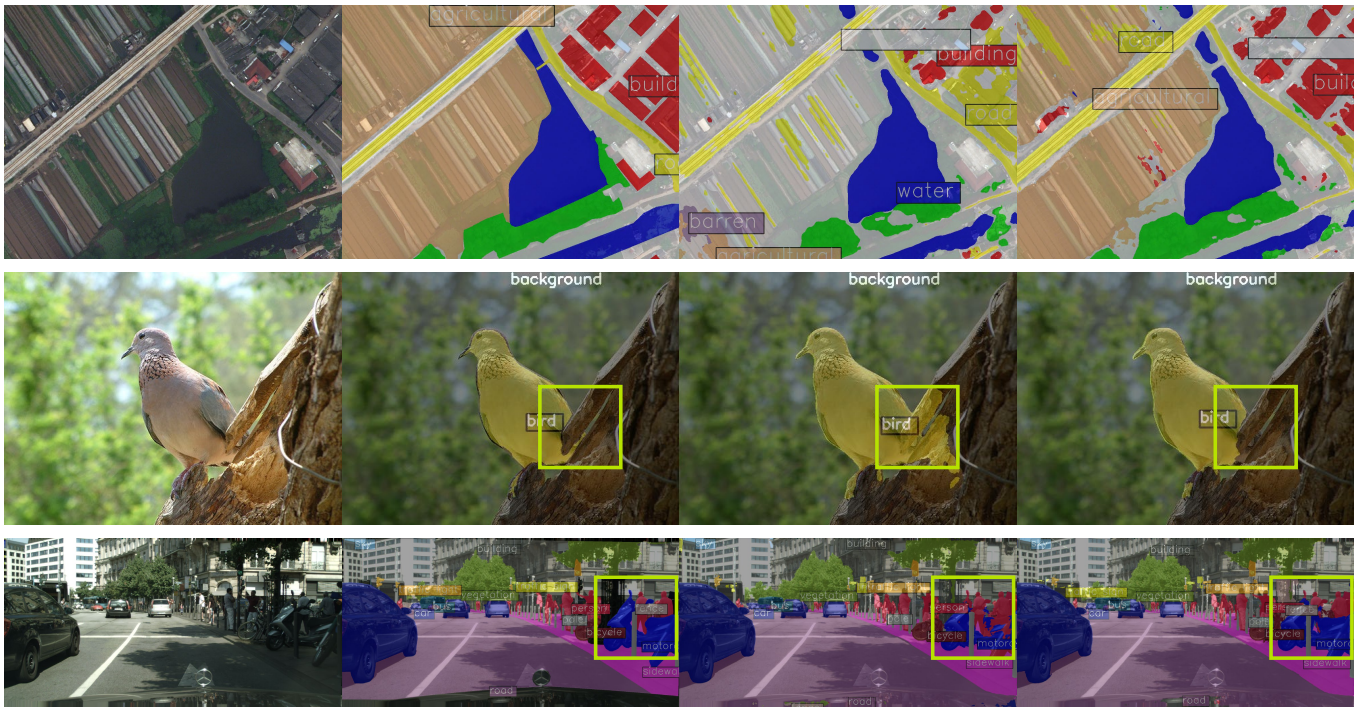

Input image Ground truth VMamba EQ-VMamba

Fig. 3. Visual comparison of segmentation results between VMamba and EQ-VMamba on LoveDA, PASCAL VOC 2012, and Cityscapes datasets.

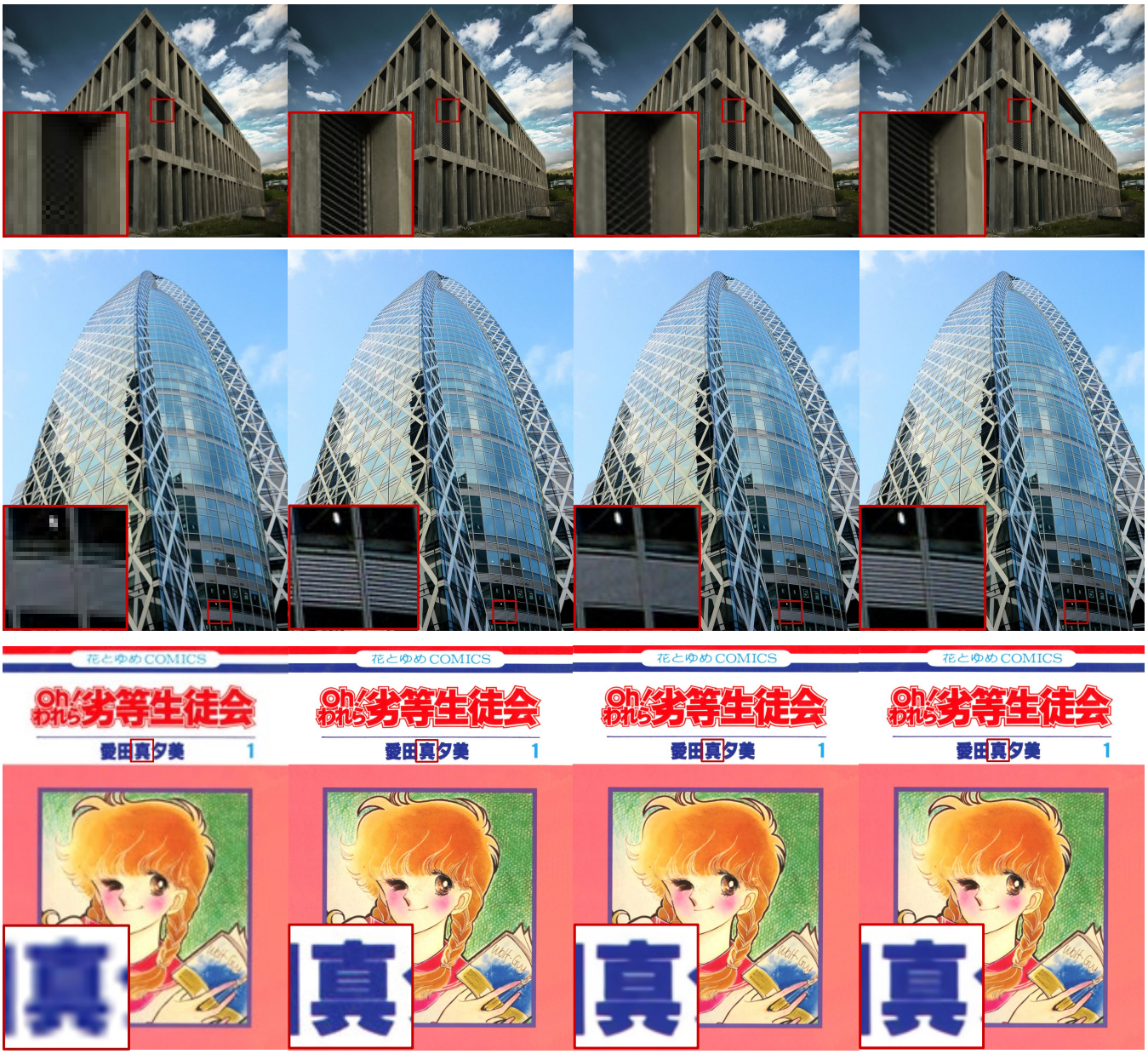

Low resolution image | Ground truth | MambaIR | EQ-MambaIR

Fig. 4. Visual comparison of image super-resolution results between MambaIR and EQ-MambaIR on the Urban100 and Manga109 datasets.

REFERENCES

[1] Siamak Ravanbakhsh. Universal equivariant multilayer perceptrons. In *International Conference on Machine Learning*, pages 7996–8006. PMLR, 2020.

[2] Qi Xie, Jiahong Fu, Zongben Xu, and Deyu Meng. Rotation equivariant arbitrary-scale image super-resolution. *IEEE Transactions on Pattern Analysis and Machine Intelligence*, 2025.

[3] Taco Cohen and Max Welling. Group equivariant convolutional networks. In *International conference on machine learning*, pages 2990–2999. PMLR, 2016.

[4] Maurice Weiler and Gabriele Cesa. General e (2)-equivariant steerable cnns. *Advances in neural information processing systems*, 32, 2019.

[5] Zhengyang Shen, Lingshen He, Zhouchen Lin, and Jinwen Ma. Pdo-econvs: Partial differential operator based equivariant convolutions. In *International Conference on Machine Learning*, pages 8697–8706. PMLR, 2020.

[6] Qi Xie, Qian Zhao, Zongben Xu, and Deyu Meng. Fourier series expansion based filter parametrization for equivariant convolutions. *IEEE Transactions on Pattern Analysis and Machine Intelligence*, 45(4):4537–4551, 2022.

[7] Radu Timofte, Eirikur Agustsson, Luc Van Gool, Ming-Hsuan Yang, and Lei Zhang. Ntire 2017 challenge on single image super-resolution: Methods and results. In *Proceedings of the IEEE conference on computer vision and pattern recognition workshops*, pages 114–125, 2017.

[8] Jia-Bin Huang, Abhishek Singh, and Narendra Ahuja. Single image super-resolution from transformed self-exemplars. In *Proceedings of the IEEE conference on computer vision and pattern recognition*, pages 5197–5206, 2015.

[9] David Martin, Charless Fowlkes, Doron Tal, and Jitendra Malik. A database of human segmented natural images and its application to evaluating segmentation algorithms and measuring ecological statistics. In *Proceedings Eighth IEEE International Conference on Computer Vision. ICCV 2001*, volume 2, pages 416–423. IEEE, 2001.

[10] Roman Zeyde, Michael Elad, and Matan Protter. On single image scale-up using sparse-representations. In *Curves and Surfaces: 7th International Conference, Avignon, France, June 24-30, 2010, Revised Selected Papers 7*, pages 711–730. Springer, 2012.
[11] Marco Bevilacqua, Aline Roumy, Christine Guillemot, and Marie Line Alberi-Morel. Low-complexity single-image super-resolution based on nonnegative neighbor embedding. 2012.
[12] Yulun Zhang, Kunpeng Li, Kai Li, Lichen Wang, Bineng Zhong, and Yun Fu. Image super-resolution using very deep residual channel attention networks. In *Proceedings of the European conference on computer vision (ECCV)*, pages 286–301, 2018.